Correlation between physical properties and electrochromic performances of DC magnetron sputtered a-WO_x thin films

K. B. Joël-Igor N'Djoré [a, b], M. Grafouté[a], A. Bulou[c] C. Rousselot[*b]

[a] Université Félix Houphouët Boigny, Laboratoire de Technologie, UFR SSMT 22, BP 258 Abidjan, Côte d'Ivoire

[b] Université de Franche Comté, Institut FEMTO-ST (CNRS/UFC/ENSMM/UTBM), Département MN2S, BP 71427, F-25211 Montbéliard cedex, France

[c.]Le Mans Université, Institut des Molécules et Matériaux du Mans (CNRS UMR6283), F-72085 Le Mans cedex 09, France

*Corresponding author: C. Rousselot (Christophe.rousselot@univ-fcomte.fr)

4, place Tharradin 25211 Monbéliard Cedex, France, (+33) 381 994 714)

Abstract

Tungsten oxide thin films were grown on different substrates by the conventional process of direct current magnetron sputtering. A series of amorphous WO_x (a-WO_x) films, with variable stoichiometry and porosity, were achieved with different total pressure (P_t) induced by oxygen flow rate ($Q(O_2)$) variation. The objective of this study is to determine the couple ($Q(O_2)$; P_t) necessary to achieve optimal electrochromic performances of WO_x and also study the correlation between physical properties and electrochromic performances. The WO_x films optical transmittance evolved from opaque to transparent with the increase of $Q(O_2)$. A degradation of films refractive index and the increase of their porosity, both mainly due to the increase of P_t, were observed. The Raman spectroscopy indicated the presence of different W valence states in the as deposited a-WO_x films. They all contain W^{4+}, but W^{6+} were found only into transparent or semi-transparent films. A weak peak of W^{5+} was observed into the semi-transparent film. Electrical properties studied by Metal-Oxide-Semiconductor structures showed a decrease of the oxide capacitance when $Q(O_2)$ and P_t increase. The WO_x transparent and optically reversible films, deposited with lower values of ($Q(O_2)$; Pt), i.e., $Q(O_2)$ = 4.5 sccm and 6 sccm, and P_t = 1.13 Pa and 1.37 Pa, respectively, exhibited the highest values of WO_x/Si interface traps average density and positive ions density (N_{ss}). The positive N_{ss} reflects the oxygen deficiency amount in the films. These films were resistive to the discoloration process but showed the highest coloration efficiency CE_{632nm} = 44.4 cm^2/C and 42.2, respectively. Their coloration times were t_c = 19 s and 22 s, and their discoloration times were t_d = 180 s and 75 s, respectively. They exhibited the highest optical modulation close to ΔT_{632nm} = 76 %.

Key words

- WO_x thin films
- Direct Current magnetron sputtering
- Optical properties
- Electrical properties
- Metal-Oxide-Semiconductor structures
- Raman spectroscopy
- Electrochromic performances

Highlights

- WO_x thin films ($0 < x \leq 3$) deposited by DC reactive magnetron sputtering
- Variation of the porosity and the stoichiometry of WO_x films by total pressure and $Q(O_2)$
- Optical, electrochromic and electrical properties studied and correlated with $Q(O_2)$
- Electrochromic properties are correlated to electrical parameters such as D_{it} and N_{ss}
- Raman study reveals different valence states, W^{4+}, W^{5+} and W^{6+} depending of $Q(O_2)$

1 Introduction

Electrochromic materials are able to change their optical properties under the action of an electrical voltage. This change of optical properties when a voltage is applied across electrochromic materials is called electrochromism [1]. Electrochromism for cathodic coloring materials, often transition metal oxides, is based on a double injection/extraction of electrons and cations in/from their structure according to the following redox equation [2]:

$$\underset{\text{(Transparent)}}{MO_y + x\,C^+ + x\,e^-} \rightleftharpoons \underset{\text{(Colored)}}{C_xMO_y} \qquad \text{(eq. 1)}$$

where M is a transition metal (W, Ta, Ti, etc.), C is a cation (Na^+, Li^+, H^+, etc.) and x is the fractional number of inserted ions and electrons inside the MO_y film.

Electrochromism is known to be existed in several types of transition metals oxide [2]. Among them, tungsten trioxide (WO_3) is by far the most extensively studied inorganic electrochromic material because of its cubic “perovskite-like” structure [2,3]. The free space inside the WO_3 cubic structure is considerable and provide a large number of interstitial sites where cations can be inserted. The coloration process of WO_3 is described by different models which are sometimes contradictory [4]. One of the most accepted models to explain WO_3 coloration is the intervalence charge transfer transition between W^{5+} and W^{6+} sites after the insertion of electrons and cations [5,6]. WO_3 coloration is also explained by small polaron absorption [7]. As WO_3 optical transmittance is reversible, the disinsertion of electrons and cations allows this material to retrieve its initial transparent state. Due to its optical change, the WO_3 thin film can be integrated in devices that modulate their transmittance, reflectance or absorptance [8,9]. Tungsten oxide thin films are generally used as an active layer in several

optoelectronics devices such as architectural glazing, display screen, sun roof, solar glass and smart windows [1,8,10]. A large variety of deposition techniques like thermal evaporation [11], spray pyrolysis [12], chemical vapor deposition [13] and magnetron sputtering [14] have been utilized to obtain WO_3 thin films.

According to literature [15,16], amorphous WO_3 thin films with relatively porous microstructure and larger thickness exhibit optimal electrochromic (EC) performances, good optical reversibility and smallest coloration/bleaching time. Porous films can be obtained with high total pressure during deposition and amorphous films are generally deposited at room temperature [15]. For Yu et al. [17] and Lee et al. [18], amorphous and sub-stoichiometric WO_{3-y} films exhibit better optical modulation and coloration efficiency. So, the attractive EC performances are due to the synergistic effects of the porosity and oxygen vacancy (or deficiency) in the WO_x [19]. Therefore, the choice of the deposition technique, deposition conditions and parameters are of a great importance to achieve an electrochromic material with optimal performances.

The oxygen vacancy defects are supposed to increase WO_x conductivity and influence their electrochromic performances [20]. But since O-rich WO_x films are electrically resistive, it is difficult to measure their conductivity or resistivity with a classic 4-probes device. The oxide films electrical properties in this study will be studied from Metal-Oxide-Semiconductor (MOS) structures. Indeed, the electrical characteristics of the MOS structures can help us to assess defects in oxides films [21]. In WO_x films, these defects accessible from a MOS structure are of a great importance in the understanding of their electrochromic behavior. The WO_x electrical properties studied by MOS structures is not widespread in the literature and their correlation with electrochromic performances is not well-known.

In this study, we sputter-deposited WO_x films by Direct Current (DC) magnetron sputtering with different oxygen flow rates ($Q(O_2)$) and total pressures (P_t) in order to modulate their stoichiometry and porosity, necessary for the optimization of their electrochromic performances. We also examine the influence of $Q(O_2)$ and P_t on optical and electrical properties and the correlation of these properties with the electrochromic performance of WO_x films. We will emphasize on the correlation between electrical properties and electrochromic performances of WO_x. The ions density (N_{ss}) and the interface traps density distribution (D_{it}) at the interface WO_x/Si, constitute the main electrical parameters, which will be correlated to the electrochromic performance, such as the coloration efficiency and the kinetics of ions insertion/extraction in/from WO_x structure.

2 Experimental procedures

2.1 WO_x films deposition

Tungsten oxide films were deposited by DC magnetron sputtering of a W target (purity 99.9 % and diameter 2'') in a gas mixture of Argon and oxygen. A constant current of 0.1 A was applied to the W target. Reactive sputtering experiments were performed using a vacuum reactor (Alliance Concept AC 450) of 70 L. Before introducing constant Ar and O_2 gas flow rates in the reactor, a base pressure of 10^{-4} Pa was obtained with a turbomolecular pump backed with a mechanical one. The pumping speed during deposition process was 10 L s^{-1}. Amorphous films were deposited on glass and SnO_2 substrates at room temperature using different total pressures and different constant oxygen flow rates for an Ar pressure maintained at 0.41 Pa. The substrates were cleaned with ethanol and dried at room temperature before each sputtering process. The glass/SnO_2 substrates were ultrasonically cleaned during 8 minutes to remove eventual soils, then rinsed in distilled water and finally dried at room temperature. For each

deposition, all deposit parameters were recorded using the deposit monitoring software. The WO_x thin films thickness deposited onto glass substrates were measured using a Dektak 3030 profilometer. In table 1, we have listed the oxygen flow rates, total pressures, oxygen stoichiometries and all the films thickness deposited on glass or glass/SnO_2 substrates.

2.2 Characterizations

The content in O_2 and W atom in deposited films was obtained by Energy Dispersive X-Ray Spectroscopy (EDS). For this purpose, we used an OXFORD detector in the FEG JEOL 7610 F microscope. To achieve the quantitative analysis of O_2 and W in the films, K_α-line (0.525 eV) and M_α-line (1.775 eV) signals were used respectively. The acceleration voltage and the current for the EDS measurements were 5 kV and 100 nA. The atomic ratios of oxygen and tungsten present in the deposited films, are shown in Table 1.

The SEM (Scanning Electron Microscope) measurements were carried out in order to observe the morphology of the deposited films. Before the SEM analyses, the samples were covered with a thin metallic layer of chromium (20 nm of Cr) in order to ensure the electrical conductivity of the samples and to avoid any drift due to charging effects during the FIB cutting process (Focused Ion Beam). This Cr deposit was carried out by magnetron sputtering in a Leica ACE 600 metallizer. The samples were then installed in a dual-beam SEM/FIB station, Helios Nano lab 600i from FEI. The FIB column generates a focused Ga^+ ion beam in order to obtain a cross-section of the sample.

Structural X-Ray Diffraction (XRD) analyzes reveal no peak characteristic of a crystallized WO_3 structure. It can therefore be confirmed that all the a-WO_x films deposited at room temperature are amorphous (see the insert of Figure 1.b).

Raman spectroscopy study was carried out on a-WO_x thin films of about 500 nm of thickness deposited onto glass substrates in order to determine the chemical bonding configuration and W valence states. The Raman scattering spectra were collected with a T64000 multichannel spectrometer (Horiba-Jobin-Yvon) using a Si-based CCD detector cooled to –133°C (liquid nitrogen-cooled). The experiments were performed under optical microscope, (Olympus BX41), in the backscattering geometry, with a X50 LF objective (numerical aperture 0.5) and using as excitation the 514.5 nm wavelength radiation (Ar/Kr Coherent Spectrum laser) with power limited to 0.6 mW on the sample. The spectra were collected in a broad wavenumber range, from 120 cm^{-1} to 3500 cm^{-1} (single monochromator and 600 tr/mm grating/1.8 cm^{-1} instrument resolution), and close to the low wavenumbers, from 20 cm^{-1} to 1500 cm^{-1} (triple monochromator and 1800 tr/mm grating/ 0.7 cm^{-1} instrument resolution). They were calibrated with the 520.2 cm^{-1} line of a silicon wafer and corrected from glass substrate signal. The Raman spectra wavenumbers, intensities, and widths were then fitted by Labspec5 software using a combined Lorentzian-Gaussian band shape.

Films deposited on glass substrates were characterized by optical transmission spectroscopy with normal incidence, measured with a Perkin Elmer lambda 950 spectrophotometer, in the wavelength range from 200 nm to 1,100 nm, in order to draw their transmission spectrum. For each spectrum, the refractive index of each WO_x films is determined from the interference fringes, using the Swanepoel method [22,23].

For electrical study, films with only about 200 nm were deposited onto n-type Si wafers (100) with a resistivity of 1-20 Ω.cm and a carrier concentration of 10^{14}-10^{15} cm^{-3}. The electrical measurements were performed with a mercury probe capacitance meter. The electrical procedure measurement with this capacitance meter, is widely detailed in our previous paper [24]. Electrical characteristics studied in this work were the oxide capacitance (Cox), the

hysteresis of the capacitance-voltage curve: C-V (ΔV), the interface traps density distribution (D_{it}) [25,26] at WO_x/Si interface and ions density (N_{ss}). The D_{it} and N_{ss} are calculated from the indications given by N'Djoré et al [24]. Cox is measured in accumulation regime. Hysteresis is determined by applying a back-and-forth gate voltage across the MOS structures. The voltage evolves from 0 V toward negative voltages, then reverse to positive voltages and end at 0 V. Among the methods that exist to quantify defects in the volume of oxide films, we used the hysteresis loop of C-V curves by applying a back-and-forth gate voltage (V_g) with a frequency of 1 MHz across MOS structures. The mid-height width of the hysteresis loop of C-V curve, appointed ΔV, is representative of defects in the volume of WO_x films [21].

Thin films of WO_x with about 500 nm [27] of thickness were deposited onto glass/SnO_2 substrates for electrochromic study. The SnO_2 has a square resistance of 26 Ω/□. After deposition of WO_x films, electrochemical analyses were performed with a three electrodes electrochemical cell. The electrochemical cell is composed of a working electrode (glass/SnO_2/WO_x) with a contact surface of 2 cm x 1.5 cm = 3 cm^2, a saturated reference electrode Hg/Hg_2Cl_2/KCl, noted SCE (Saturated Calomel Electrode) and a counter electrode which consist of a platinum grid. The three electrodes were immersed in a 1.0 M solution of lithium perchlorate ($LiClO_4$), dissolved in propylene carbonate. Electrodes were connected to a 33V/2A potentiostat fitted with an intelligent programmable interface (IMT 101) and coupled to the VoltaMaster 2 software for data recording and processing during the cyclic voltammetry and chronoamperometry measurements. Voltammetry measurements were conducted between - 1 V and + 1 V vs SCE with the scan rate of 20 mV/s in order to observe the phenomena of intercalation and desintercalation of carriers (Li^+, e^-) through the current density-voltage (J-V) curves. Chronoamperometry measurements were done at a fix potential of - 1 V for films coloration (reduction reaction). Then, after coloration, a fix voltage of + 1 V was applied to

achieve films discoloration (oxidation reaction). Chronoamperometry measurements permitted us to evaluate films response time, optical modulation and coloration efficiency.

3 Results and discussions

In table 1, we have listed the oxygen flow rates, total pressures, oxygen stoichiometries and all the films thickness deposited on glass or glass/SnO_2 substrates. The same films (table 1), but with thickness of about 200 nm, were deposited onto silicon and in the same conditions for electrical measurements.

3.1 Optical properties and porosity

The Figure 1.a shows the WO_x optical transmission versus the wavelength for various oxygen flow rates between 1.2 and 14 sccm and (i.e., total pressure 0.45 and 2.60 Pa). The WO_x thin films average optical transmittance calculated in the visible region between 400 nm and 800 nm versus oxygen flow rate is shown also in Figure 1.b.

For Q (O_2) = 1.2 sccm ($WO_{1,92}$), the WO_x sample obtained is opaque. Its average optical transmittance is close to zero in the visible region. When Q (O_2) ≥ 1.65 sccm, films evolve from semi-transparent (bluish) to transparent with appearance of interference fringes in the visible region. The bluish film deposited with Q (O_2) = 1.65 sccm ($WO_{2.56}$), presents an average optical transmittance of 32% in the visible range. The blue aspect of the film is due to an under-stoichiometric, with considerable oxygen vacancies associated to W^{4+} and W^{5+} [28]. This under-stoichiometric permits the absorption of the photon which induce an electronic transfer from between the O valence band to the W conduction band, at the origin of the bluing. In addition, the bluing can also be attributed to an electronic inter-valence transition between W^{6+} and W^{5+}. Finally, all the WO_x films deposited with Q (O_2) ≥ 1.95 sccm have an average optical transmittance of about 80 % and are transparent with interference fringes. Indeed, the films

prepared with $Q(O_2) \geq 3$ sccm become increasingly oxygen-rich to reach the stoichiometry WO_3 at $Q(O_2) = 14$ sccm (Table 1) with a reinforcement of covalent bonds W-O. This reinforcement of W-O bonds may disadvantage the inter-atomic electronic transfer and also the electronic inter-valence transition between W^{6+}, W^{5+} and W^{4+}, reason why these deposited films are transparent.

According to Figures (1.a and 1.b) and table 1, we can assume that the transparency of films deposited between $3\ sccm \leq Q\ (O)_2 \leq 14\ sccm$ is probably due to their enrichment in oxygen and the predominance of W^{6+} as observed by Li et al.[24,29]. As a consequence, these transparent films could be potential candidates for electrochromic studies.

The refractive index (n) of WO_x thin films was determined from the refractive index of the glass substrate and the successive optical transmittance maxima and minima of optical transmittance interference fringes (Figure 1.a) by using Swanepoel's method [22,23]. Changes in oxygen flow rate and total pressure allow the formation of films with different porosities and result in different refractive indices. We choose to represent in Figure 2, the effect of total pressure on the evolution of the refractive index, only for transparent WO_x thin films. The refractive index is represented versus the wavelength with $425\ nm\ \leq \lambda \leq 800\ nm$.

Figure 2 shows a progressive decay of WO_x thin film refractive index when the total pressure in the deposition reactor increases. This result is in accordance with Sun et al.[15] study. In addition, we observe in this Figure 2 a systematic decrease of the refractive index of each WO_x thin film when the wavelength evolves from 425 nm to 800 nm. This refractive index dispersion with respect to the wavelength in visible region, is well known for transparent films and is characterized by the following Cauchy equation [30] :

$$n(\lambda) = A + B/\lambda^2 + C/\lambda^4 + \ldots \quad \text{(eq.4)}$$

Where n (λ) is the refractive index for a given wavelength, λ is the wavelength, and A, B, C are coefficients which are characteristics of the deposited films.

According to literature, the refractive index of transparent WO_x thin films depends on their density (or porosity) [15,31,32]. Since the porosity is influenced by oxygen stoichiometry and the total pressure [15], we have represented the evolution of both average refractive index and average porosity of films, as a function of total pressure and oxygen flow rate in Figure 3. The average refractive index and average porosity were calculated in visible region, precisely for $425\,nm \leq \lambda \leq 800\,nm$. First of all, we calculated the film relative density P (λ) with the Lorentz-Lorentz equation [15,32] :

$$P(\lambda) = \frac{\rho_f}{\rho_b} = \frac{{n_f}^2(\lambda)-1}{{n_f}^2(\lambda)+2} \times \frac{n_b^2+2}{n_b^2-1} \quad \text{(eq.5)}$$

where ρ_f and ρ_b are respectively the density of WO_x thin films and WO_3 bulk, n_f and n_b are the refractive index of WO_x thin films and WO_3 bulk. For WO_3 bulk, the average value of the refractive index is 2.5 [33]. The films porosity $\pi(\lambda)$ is then obtained by the following expression [34]:

$$\pi(\lambda) = 1 - P(\lambda) \quad \text{(eq.6)}$$

According to Figure 3, when total pressure and oxygen flow rate increase, the evolution of the average refractive index and of the average porosity of WO_x are inversed. The dense films show higher refractive index compared to porous films. The average refractive index of the WO_x films decreases from 2.13 to 2.03 while average porosity increases from ~ 15 % to ~ 20 % for respectively P_t = 0.61 Pa and 2.6 Pa and $Q(O_2)$ = 1.95 sccm and 14 sccm. Consequently, we can say that the decay of the average refractive index is due to the increase

of films average porosity, the latter is induced by the increase of total pressure. Some authors already attributed the decrease of WO_3 [34], Ta_2O_5 [35] and ZrO_2 [36] films refractive index to the increase of their porosity, thus confirming our results. We can also notice that the average refractive index values of WO_x thin films presented in Figure 3 are lower than that of the bulk (n_b = 2.5). This confirm that WO_x films are not dense compared to the bulk and contain porosity. Let us remember that the increase of the porosity is necessary to promote the electrochromic devices performances [37].

3.2 Morphology

SEM observations (Figure 4) were performed on cross sections of the films deposited on silicon substrates with oxygen flow rates of 1.2 sccm ($WO_{1.92}$), 4.5 sccm ($WO_{2.85}$) and 14 sccm (WO_3). The SEM observations reveal that the patterns in the WO_x films sizes seem to decrease with increasing oxygen flow rate and total pressure. In the literature, some authors [29,38] attribute this evolution of the size to the improvement in the stoichiometry of the film. Indeed, when the oxygen flow increases the film tends towards a more stoichiometric WO_3 formation. The trend of XRD peak width with changing the oxygen flow rate (and total pressure also) could be due to the progressive evolution of films stoichiometry and the modification of their microstructure (porosity). Indeed, the film deposited with $Q(O_2)$ = 14 sccm exhibited a broad peak whereas the others films exhibited narrow peaks. The larger XRD peak of $Q(O_2)$ = 14 sccm, stoichiometry close to pure WO_3, may be also due to the change in microstructure such as change in grain size as shown by SEM images and the increase of porosity. The others films are under stoichiometric and less porous.

3.3 Raman spectra

The Raman scattering spectra of four a-WO_x thin films in the range 20-1500 cm^{-1} are shown in Figure 5 for various oxygen flow rates between 1.20 and 14 sccm, together with the spectrum of crystallized (monoclinic) WO_3. All the spectra of the films exhibit broad bands structures characteristic of the amorphous state, and there is no trace of any line from crystallized WO_3, in agreement with the X-ray diffraction results. The samples prepared with the highest values of $Q(O_2)$, from 14 sccm to 1.95 sccm, exhibit very similar profiles characterized by four main bands around 960 cm^{-1}, 800 cm^{-1}, 280 cm^{-1} and 50 cm^{-1}. On the other hand, the spectra are significantly different for $Q(O_2)$ = 1.65 sccm where structures appear in the range 200-480 cm^{-1}, and drastically different for $Q(O_2)$ = 1.20 sccm. No other signal is observed up to 3800 cm^{-1} for any of these samples.

To interpret these spectra, we refer to the Raman signals of WO_x thin films with variable oxygen content reported in literature. Signals in the range 950 cm^{-1} - 965 cm^{-1} are assigned to the stretching mode of the W^{6+}=O bond of terminal (non bridging) oxygen, often observed for amorphous a-WO_3 [39–41]. One can find also an intense broad band in the range 600-900 cm^{-1} attributed to O-W^{6+}-O stretching vibrations [39–41], as deduced from comparison with crystallized WO_3 (monoclinic) where the most intense Raman lines are found at 808 and 714 cm^{-1} [42,43] (Figure 5); a weaker intensity broad band around 280 cm^{-1} is attributed to O-W^{6+}-O bending vibrations [43–47,47,48]. In addition, Lee et al. [45–47,49] showed that bands centered around 330 and 450 cm^{-1} can be attributed to O-W^{5+}-O and W^{5+}=O vibrations, respectively, and that a band centered near 220 cm^{-1} could be associated with W^{4+}-O vibrations. Bands in the 1,100-1,500 cm^{-1} range and around 3,600 cm^{-1} are usually attributed to bending vibration of the W-OH bonds and water [50].

The vibrational characteristics are deduced from fitting of the Raman spectra in the spectral range 120-500 cm^{-1} and 500-1,100 cm^{-1} (Figure 5). Figure 6 shows the refinements for the samples deposited with $Q(O_2)$ = 1.20, 1.65, and 1.95 sccm that illustrate the three different kinds of spectra. The very narrow peak at 235 cm^{-1} observed in all spectra is a contamination

by plasma line. The vibrational parameters (wavenumbers, spectral widths) of the components are summarized in Table 2 with the attribution proposed as deduced from literature. All the components exhibit gaussian profiles except the most intense band around 800 cm^{-1} that is asymmetric; this signal appears perfectly fitted by two gaussian lines, as already pointed out [41], centered at 671 cm^{-1} and 782 cm^{-1} (Figure 6). For all the samples prepared with $Q(O_2) \geq$ 1.95 sccm, this profile remains strictly unchanged (the two components having the same wavenumbers, the same widths, and the same relative intensities). This band, attributed to O-W^{6+}-O stretching is used as reference. The weak and very broad band centered at 278 cm^{-1} also keep the same spectral characteristics and strictly the same integrate intensity ratio with respect to the 671-782 cm^{-1} band for any sample with $Q(O_2) \geq 1.95$ sccm (Figure 7a), which supports its attribution to the O-W^{6+}-O bending [43–47,47,48]. This witnesses for the fact that the main part of the material (bulk) still is composed of the same $W^{(6+)}O_6$ (amorphous) network (the Raman signal being characteristic of the local arrangement). The highest frequency band, centered at 961 cm^{-1} (with a very small shoulder around 1,010-1,020 cm^{-1}), is attributed to W^{6+}=O stretching vibrations [39], the weak shoulder already reported in this frequency range, being attributed to the asymmetric stretching [51,52].

When $Q(O_2)$ = 1.65 sccm, the weak broad signal centered at 278 cm^{-1} is replaced by a more intense and structured band unambiguously composed of mainly four lines with about the same magnitudes (Figure 6). The corresponding wavenumbers agree with published works, and these components can be unambiguously attributed (Table 2) to the W^{+4}-O (221 cm^{-1}), O-W^{5+}-O (320 cm^{-1}), and W^{5+}=O vibrations; in this latter case however, the band at 430 cm^{-1} reported in literature appears in the present case as composed of two lines at 458 cm^{-1} and 423 cm^{-1}. The sample obtained with $Q(O_2)$ = 1.20 sccm exhibits the same lines plus an intense and narrow peak at 268 cm^{-1}. In these two samples, in the high frequency range the bands 671-782 and 961 cm^{-1} are less resolved for $Q(O_2)$ = 1.65 sccm, and they totally merge and strongly decrease for

$Q(O_2)$ = 1.20 sccm (Figure 6). The spectra are described by an additional signal between these bands, at 922 cm^{-1} and 885 cm^{-1} for $Q(O_2)$ = 1.65 and 1.20 sccm, respectively.

As pointed out, all the films deposited with $Q(O_2) \geq 1.95$ sccm exhibit the same lines with the same profiles. On the other hand, the ratio of intensities of the 961 cm^{-1} line with respect to the 671-782 band (i.e. W^{6+}=O / O-W^{6+}-O) continuously decreases (Figure 7a) with decreasing $Q(O_2)$, and even linearly decreases as a function of the EDS O/W ratio (Figure 7b). It can be seen also (Figures 7) that the lines at 320 cm^{-1}, 423- 458 cm^{-1} characteristic of W^{5+}-oxygen vibration, remain proportional to the (remaining) band 671-782 cm^{-1} characteristic of O-W^{6+}-O stretchings; this suggests that the W^{5+} are connected to the O-W^{6+}-O network clusters rather than to the WO_2 network. On the other hand, the line characteristic of W^{4+} at 221 cm^{-1}, strongly grows from $Q(O_2)$ = 1.65 sccm to 1.20 sccm, in agreement with the fact that the sample become close to the WO_2 stoichiometry. Figures 7 also suggest that for the highest values of $Q(O_2)$, this signal is too weak with respect to the 278 cm^{-1} line to be detected. It can be pointed out that even in this sample where the composition is close to WO_2, with a majority of W^{4+} (and still a little W^{5+} and W^{6+}), the whole Raman spectrum is weak (with almost the same magnitude as the contamination by low wavenumber rotational lines of air in the near vicinity of the surface- Figure 5). This is at least partly due to the high reflectivity of the surface (as deduced from the transmittance shown fig. 1), but also to a weak Raman scattering efficiency, presumably due to a somewhat different structural arrangement; this is also supported by the fact that the broad signal around 50 cm^{-1} always observed for high $Q(O_2)$ samples (Figure 5), corresponding to narrow lines in crystallized WO_3 , slightly decreases for 1.65 sccm, and totally vanishes for 1.20 sccm samples. The fairly sharp signal at 268 cm^{-1} and the line at 885 cm^{-1} could be characteristic of this arrangement. Incidentally, this spectrum looks like the one of crystallized WO_2 [53,54], as well as the Raman spectra of amorphous WO_3 match the spectrum of crystallized WO_3 (Figure 5), as already pointed out [41,45].

These results confirm the presence of a majority of W^{4+} ions in the film of composition $WO_{1.92}$ deposited at $Q(O_2)$ =1.20 sccm and a very low oxygen deficiency (compared to stoichiometric WO_2), reason why it appeared opaque after deposition (Figure 1). Then for $Q(O_2)$ = 1.65 sccm, the film contains W^{5+} in addition to the W^{4+}, and W^{6+} valence states, with an intermediate stoichiometry between WO_2 and WO_3. The presence of W^{5+} ions in this film seems to be the cause of its bluish color (Figure 1). There is a majority of W^{6+} ions, which is responsible for their transparency (Figure 1).

3.4 Electrical properties

The electrical parameters presented in this section such as C_{ox}, N_{ss}, $D_{it\text{-}average}$ and the ΔV are determined form capacitance-voltage (C-V) curves obtained during a previous study [24].

3.4.1 WO_x capacitance

The evolution of the C_{ox} of WO_x films versus oxygen flow rate is showed in Table 3. According to this Table 3, the WO_x thin films C_{ox} is influenced by the oxygen flow rate. The capacitance globally decreases from C_{ox} = 8,88 x 10^{-10} F to 4.01 x 10^{-10} F when Q (O_2) increases from 1.2 sccm to 14 sccm. The C_{ox} values of WO_x films can be compared to the values obtained by Tutov [55]. We can observe that the O-rich films present lower values of C_{ox} compared to the film synthetized with 1.2 sccm. The decay of the C_{ox} when Q (O_2) increases may be mainly due to the resistive nature of O-rich films [56]. We must precise that total pressure and porosity may influence the evolution of the C_{ox}, but we still do not know how.

3.4.2 Defects and ions density in WO_x films

Defects result from the growth conditions of the oxide. In this work, we will focus on WO_x intrinsic defects which are due to the arrangement of oxygen and tungsten atoms in the films. Intrinsic defects can appear as interstitials, substitutions, or as oxygen vacancies associated with contracted, broken or dangling bonds [21,26]. These defects are present in the volume of WO_x, close to the interface or at the interface WO_x/S_i. A defect can be electrically active and can behave like a trapping site when it captures a charge carrier or like a site of recombination when it can exchange a charge carrier with the oxide valence or conduction bands [57,58].

Various methods exist to quantify defects in oxide films. In our study, we used the hysteresis loop of C-V curves by applying a back-and-forth gate voltage (V_g) with a frequency of 1 MHz across MOS structures. The hysteresis is a common phenomenon in the dielectrics (oxides) and is considered to be due to charge trapping [21,59]. The mid-height width ΔV of the hysteresis loop is representative of defects in the volume of WO_x films which are not in contact with the substrate. More ΔV amplitude is important, more defects in the volume of WO_x films are important. Also, we determine the WO_x/Si interface traps or states density distribution (D_{it}) by Terman method [25,26,60]. The interface trap is a defect that lies precisely at the oxide/semiconductor interface, and can communicate electrically with the underlying semiconductor [21]. For Terman, at an oxidized semiconductor surface, the transition from ordered semiconductor crystal lattice to the oxide layer represents a major discontinuity which will result in dangling or unsaturated bonds [26]. The interface traps are similar to defects found in the volume of the oxide.

As seen, oxygen vacancies in WO_x films are considered as defects measurable taking into account in the measurements of D_{it} and also ΔV. When the oxygen flow rate increases, the evolution of these oxygen vacancies can be reflected by the evolution of the N_{ss} in the WO_x

films. The N_{ss}, ΔV, and $D_{it\text{-}average}$ for all WO_x films are shown in Table 3. As an example of determination of ΔV, we show in Figure 9 the hysteresis loop of films deposited with Q (O_2) = 8 sccm.

According to the data of Table 3, a negligible hysteresis loop and the lowest $D_{it\text{-}average}$ are observed for the sample elaborated with 1.2 sccm. The result reflects a good interface WO_x/Si quality [61]. This film $WO_{1.92}$ which contains mainly W^{4+} valence states, exhibits the smallest number of positives ions N_{ss}, so a small number of oxygen vacancies. This opaque film is close to stoichiometric WO_2 and is not desirable for electrochromic device. Beyond Q (O_2) = 1.20 sccm, the ΔV and $D_{it\text{-}average}$ of each WO_x films increase progressively to reach the highest value when the oxygen flow rate is 3 sccm. This evolution reflects a progressive increase of defects in the volume and a degradation of the interface quality in these films. Moreover, the increase of defects is followed by the formation of a large number of positives ions (increase of N_{ss}) due to a large number of oxygen vacancies associated to W^{4+}, W^{5+}, and W^{6+} valence states. Since these films evolved from semi-transparent to transparent, W^{5+} are present in the semi-transparent film prepared with Q (O_2) = 1.65 sccm and W^{6+} are preponderant in the transparent films synthetized with 1.95 sccm and 3 sccm of oxygen flow rate (Table 2). Above Q (O_2) = 3 sccm, ΔV which reflects the defects in the volume seems to be less influenced by the increase of Q(O_2). On the other hand, $D_{it\text{-}average}$ decreases progressively with the increase of Q(O_2) showing thus, a progressive reduction of the defects of interfaces with improvement of the quality of the interfaces. The N_{ss} also gradually decreases, reflecting the decrease of oxygen vacancies in these films. This decrease of oxygen vacancies may explain the decay of $D_{it\text{-}average}$. The negative value of N_{ss} for the film prepared with Q (O_2) = 14 sccm is representative of a stoichiometric or over-stoichiometric WO_3. The W^{6+} valence states associated with a decrease of oxygen vacancies, is preponderant in the films elaborated with 4.5; 6; 8 and 14 sccm of oxygen flow rate. These transparent films seem to be interesting for electrochromic devices.

Finally, $Q(O_2)$ = 3 sccm seems to be the critical value beyond which we can make transparent WO_x with nearly constant volume defects whatever $Q(O_2)$ ($1.7 < \Delta V < 2$). On the other hand, for $Q(O_2)$ > 3 sccm the interface defects (D_{it}) and the oxygen vacancies (N_{ss}) decrease as the oxygen flow rate increases, improving thus, the quality of the interfaces and the stoichiometry (Table 1). The possibility to vary both the defects and the stoichiometry seems promising in the optimization of the electrochromic properties.

3.5 Electrochromic study

3.5.1 Cyclic voltammetry

Electrochromic measurements were not possible in our electrochemical windows [-1V; +1V] for films deposited with Q (O_2) ≤ 3.0 sccm. This is due to their insufficient content in oxygen, their relatively dense microstructure [62,63] and their opacity. Figures 9 a-d show the first and fifth cyclic voltammograms recorded at 20 mV/s for films deposited with 4.5; 6; 8 and 14 sccm of oxygen flow rate, respectively. The scan was started at 0.25 V (vs. (Saturated Calomel Electrode) SCE) and continued towards negative voltages. The current density is close to zero until the potential drops below - 0.15 V (vs. SCE) from which the current density becomes progressively negative. This cathodic branch corresponds to intercalation, where electrons from the SnO_2 electrode and Li^+ ions from the electrolyte are co-inserted into the WO_x films. As soon as the current density changes from negative to positive values, after reversing the scan direction from -1.0 V (vs. SCE), deintercalation starts during this anodic branch. The deintercalation current passes through a maximum and finally becomes approximately zero, after reversing the scan direction from +1.0 V (vs. SCE), to a potential return close to 0.25 V (vs. SCE).

During the 1^{rst} J-V measurement, Figures 9a-d show an important insertion of charge carriers into WO_x films reflected by an important cathodic current density whose slope of -2 mA/V is nearly constant for all films. But surprisingly, no coloration and discoloration were observed with eyes despite this constant speed of cathodic insertion. For some authors [64,65], the observed phenomenon during the 1^{rst} J-V measurement for over-stoichiometric films (3.3 < O/W ratio < 3.5) can be attributed to the formation of neutral compound Li_2O_i called Lithia. In these films, the excess oxygen is incorporated as interstitials in the structure of the film, and can serve as trapping centers for lithium during the co-insertion of lithium ions and electrons. As far as we are concerned, the films being under-stoichiometric (Table 1), we can rather partially explain this phenomenon by the presence of defects in WO_x films. These defects are electrically active and can behave like trapping or recombination sites. Therefore, during the first insertion, we think that most of the charge carriers are trapped in these defects so that reduction of W^{6+} to W^{5+} does not occur. Moreover, as the volume defects in these films are almost constant with approximately the same ΔV (Table 3), then the cathodic insertion rate and the cathodic current density during the first J-V cycle are close for all the films. After several J-V measurements, most of the trapping sites or defects are saturated and the J-V voltammograms become stable from the 5th J-V measurement with an electrical reversibility (ER) above 90 %. Therefore, during the cathodic scan, a reduction from W^{6+} to W^{5+} occurs in transparent WO_x thin films which become dark blue. Otherwise, during the anodic scan, an oxidation from W^{5+} to W^{6+} resulting in the original transparent state of the films occurs. Electrochemical reaction allows the coloration/discoloration when both Li^+ and e^- are electrochemically intercalated/deinterlaced in WO_x thin films

As we can see on the Figures 9 a-d, surfaces delimitated by the 5th J-V curves are not the same, especially in anodic branch and depend on $Q(O_2)$. This reflects different number of

charges intercalated and deintercalated for each film. Films indicate a cathodic branch where the current density is negative between - 0.15 V and - 1 V during coloration or reduction process. During discoloration or oxidation process, the anodic branches with positive current density for films deposited with Q (O_2) = 4.5 sccm (Figure 10a) and 6 sccm (Figure 10b) are flat and very spread out up to +1 V (vs. SCE). This reveals a relatively slow discoloration kinetics of these films which seem resisting to Li^+ and e^- disinsertion. This slow discoloration kinetics and this difficulty in bringing out the charge carriers can be explained by the combined effects of the presence of numerous interface defects revealed by the highest values of the $D_{it\text{-}average}$ (Table 3), by oxygen deficiency reflected by a higher positive ion density (N_{ss}) (Table 3) and by their relatively dense microstructure (lower porosity Figure 3).

In comparison, the anodic branches of films elaborated at 8 sccm (Figure 10c) and 14 sccm (Figure 10d) of oxygen flow rate, are rounded and stop quickly before + 0.25 V (vs. SCE). This reveals a relatively rapid discoloration kinetics of these films which seem sensitive to Li^+ and e^- disinsertion with a rapid discoloration. This sensitivity can be attributed to the combined effects of the decrease of the $D_{it\text{-}average}$, of oxygen deficiency reflected by N_{ss} (Table 3) and to their porous microstructure (Figure 3).

3.5.2 Chronoamperometry

Figures 10 a-b present the evolution of the current density vs time during insertion (coloration) or disinsertion (discoloration) of charges. All the films were colored during 30 s (Figure 11 a). At the beginning of the coloration process (t = 0 s - 2.5 s), the films exhibit different cathodic current density which increase with oxygen flow rate and revealing that the films close to stoichiometry, the most porous with the least defects exhibit the highest insertion kinetics. This is in accordance with the evolution of porosity, of stoichiometry and defects in

the films as a function of Q (O_2). The current density tends to stabilize around – 0.5 mA/cm^2 towards t = 30 s for all the films, reflecting thus, a slowing down of the co-insertion (Li^+ and e^-) and of the coloring rate. During discoloration, Figure 11b indicates a faster decay in the current's density for films deposited with 8 sccm and 14 sccm of oxygen flow rate compared to films deposited with Q (O_2) = 4.5 sccm and 6 sccm. This reveals that the disinsertion rate is favored by a high porosity, a minimum of interface defects and a low deviation from the stoichiometry of the films.

These results suggest that bleaching and coloration kinetics are faster for higher Q (O_2) films as already observed during cyclic voltammetry measurements.

3.5.2.1 Optical modulation

The optical transmittance versus wavelength of WO_x thin films at colored and bleached state during the chronoamperometry measurements are shown in Figures 11 a-d for all films deposited with Q (O_2) =4.5, 6, 8 et 14 sccm, respectively. We performed ex-situ optical measurements. As seen, transmission decreases sharply as WO_x films are darkened. According to Figure 12, all deposited films are optically reversible. We must precise that, in Figures 11 a-d, dash lines for bleached state represent the initial optical transmittance of as deposited a-WO_x films. In the Figure 12, we can notice a shift and superposition of the absorption threshold of colored and bleached films toward smaller wavelengths reflecting a modification of their bandgap after intercalation/deintercalation of charges. Optical modulation (ΔT), which is the difference of optical transmittance between the bleached and the colored states of films is also shown on this Figure 12 for λ = 632 nm [66,67]. The ΔT of films are very close after 30 s of insertion. It can be explained by the fact that the current density reached after 30 s during coloration process is close to 0.5 mA/cm² for all the films, despite different kinetics of insertion. On the other hand, to reach the optical reversibility during the disinsertion of the films (ΔT discoloration), the times required are very different, revealing slower discoloration kinetics for the lowest Q(O_2).

3.5.2.2 Coloration efficiency (CE)

One quantitative way to characterize the color change in electrochromic materials is to calculate their coloration efficiency (CE). The CE is then, an important index to follow during the fabrication of electrochromic devices. This parameter is given by [68,69]:

$$CE = \frac{\Delta OD}{Q_{in}} \quad \text{(eq.8)}$$

Where CE (cm^2/C) is the coloration efficiency, Q_{in} (C/cm^2) is the injected charges quantity into the film per unit area and ΔOD is the optical density change. The optical density means the light absorption ability of electrochromic films during their 2 extremes optical states. ΔOD is calculated with the following equation:

$$\Delta OD = \log(\frac{T_b}{T_c}) \quad \text{(eq.9)}$$

where T_b and T_c are the transmissions in the bleached and the colored states, respectively. A high CE indicates that the material structure exhibits a large optical modulation with a small charge insertion. The evolution of CE versus wavelength is given in Figure 13. It can be seen from the Figure 13 that the coloration efficiency of WO_x films decreases with increasing oxygen flow rate and tend to increase vs wavelength in the visible region, for all the films. The maximum coloration efficiency is reached at 770 nm. The decay of the CE for films prepared with 8 sccm and 14 sccm of oxygen flow rate, could be due to their higher porosity close to 20 %, but mainly to the decrease of oxygen deficiency. Probably, their porous microstructure does not enable availability of enough insertion sites for Li^+ ions intercalation to form the tungsten bronze. The coloration efficiency of these films at 632 nm are 33.0 cm^2/C and 34.3 cm^2/C,

respectively. The highest CE values are found to be 44.4 cm^2/C and 42.2 cm^2/C at 632 nm for respectively Q (O_2) = 4.5 sccm and 6 sccm, P_t = 1.13 Pa and 1.37. These WO_x films CE is improved firstly because of their less porous microstructure (Figure 3) as it was also observed by Sun et al. [15]. Their less porous microstructure may allow the availability of Li^+ insertion sites in order to generate a large number of W^{5+}. Otherwise, the main reason for having highest CE with these films is their large number of positive N_{ss} associated to oxygen vacancies (Table 3). According to Lee at al. [18], the CE increases with increasing oxygen vacancies in WO_x films and this permit to generate a great number of W^{5+} by insertion of Li^+ and e^-. As shown in Figure 14, showing the evolution of the electrical parameters and the CE at 632 nm as a function of Q(O_2), one can note an interesting correlation between the interface defects (Dit) and oxygen deficiency (N_{ss}) in the films and their coloration efficiency (CE). Other authors confirm that CE changes can be guided by controlled manipulation of oxygen vacancies in films of perovskite structure without additional Li^+ ion involvement [70].

These films, with improved CE, have the highest $D_{it\text{-}average}$ and N_{ss}. As a consequence, we can assume that the control of these electrical parameters can contribute to the enhancement of the CE of WO_x.

3.5.3 Response time

The response time, which measure the time interval necessary for switching between the two extreme optical states of films, were determined by the CA. In our study, the coloration time t_c correspond in the time required to reach a variation in optical density $\Delta OD = 0.3$ at the wavelength of 632 nm. The $\Delta OD = 0.3$ correspond to a decay of 50 % of the transmission during coloration. The discoloration time t_d corresponds in the time required to return to the

initial discoloration state. t_d, is determined when the current density begin to stabilized and is close to zero (Figure 11). These response times are summarized in Table 4.

All the films of this study deposited with $Q(O_2) \geq 4.5$ sccm show staining times substantially close to 20-30 seconds to reach $\Delta DO = 0.3$. On the other hand, the discoloration times are very different from 180 to 8 seconds and seem to be strongly dependent both on interface defects and on the density of positive ions (or oxygen deficiency) present in the WO_x films. Films deposited with 8 sccm and 14 sccm of oxygen flow rate, exhibit short response time de 8 - 9 s contrarily to those deposited with $Q(O_2) = 4.5$ sccm and 6 sccm, 180 and 75 s respectively. The response time confirm observations made in section 3.4.1 and 3.4.2.

4 Conclusion

This work permitted us to show the effect of oxygen flow rate and total pressure on physical properties of WO_x thin films. The correlation between these properties and electrochromic performances of WO_x was clearly illustrated.

The WO_x optical transmittance evolves progressively from opaque to transparent when films become rich in oxygen. Also, the optical transmittance has been useful to investigate on the porosity of transparent films. Transparent films deposited with a high total pressure were porous with degraded refractive index whereas transparent films deposited with low total pressure where less porous with high refractive index. Thanks to Raman spectroscopy, we have been able to prove the existence of different W valence states and the link between transparency and the W^{6+} valence state. The C_{ox} and D_{it} of the films decrease with increasing $Q(O_2)$ and P_t.

Also, the N_{ss} decreases with increasing $Q(O_2)$ and tend to become negative with an excess of O_2 in the films.

Electrochromic performances study was possible for films deposited with $Q(O_2) \geq 4.5$ sccm and $P_t \geq 1.13$ Pa, in an electrochemical windows [-1 V; +1V]. Results show that the lowest values of ΔT, CE and a rapid insertion/disinsertion kinetics were achieved for films deposited with high ($Q(O_2)$; P_t). These films are porous with low refractive index. They exhibit a low $D_{it\text{-}average}$ and low positive N_{ss}, or a negative N_{ss}.

Otherwise, highest values of ΔT and CE, with slow insertion/disinsertion kinetics were achieve for films deposited with low ($Q(O_2)$; P_t). These films are slightly less porous with high refractive index. They exhibit higher values of $D_{it\text{-}average}$ and positive N_{ss}. A reduction of a large number of W^{6+} to W^{5+} is supposed to be formed during a double insertion of Li^+ and e^- in these films.

Finally, we have shown in this study, a correlation between the electrical parameters, the optical properties and the electrochromic performances. Since the $D_{it\text{-}average}$ reflects defects at interface and N_{ss} the oxygen deficiency, we think that a good control of these parameters, is of a great interest for the manufacturing of electrochromic devices with optimized coloration efficiency.

Acknowledgements and funds

This work was made possible thanks to the financial aid of the Pays Montbéliard Agglomération (PMA) and Côte d'Ivoire government.

References

[1] R.J. Mortimer, D.R. Rosseinsky, P.M.S. Monk, Electrochromic Materials and Devices, John Wiley & Sons, 2015.
[2] C.G. Granqvist, Handbook of Inorganic Electrochromic Materials, Elsevier, 1995.
[3] L.E. Depero, S. Groppelli, I. Natali-Sora, L. Sangaletti, G. Sberveglieri, E. Tondello, Structural Studies of Tungsten–Titanium Oxide Thin Films, Journal of Solid State Chemistry. 121 (1996) 379–387. https://doi.org/10.1006/jssc.1996.0051.
[4] K. Bange, Colouration of tungsten oxide films: A model for optically active coatings, (1999). https://doi.org/10.1016/S0927-0248(98)00196-2.
[5] R.S. Crandall, B.W. Faughnan, Dynamics of coloration of amorphous electrochromic films of WO3 at low voltages, Appl. Phys. Lett. 28 (1976) 95–97. https://doi.org/10.1063/1.88653.
[6] A. Deneuville, P. Gérard, R. Billat, Principles and operation of an all solid state electrochromic display based on a-"WO3," Thin Solid Films. 70 (1980) 203–223. https://doi.org/10.1016/0040-6090(80)90361-2.
[7] O.F. Schirmer, E. Salje, The W5+ polaron in crystalline low temperature WO3 ESR and optical absorption, Solid State Communications. 33 (1980) 333–336. https://doi.org/10.1016/0038-1098(80)91164-3.
[8] C.G. Granqvist, Oxide electrochromics: Why, how, and whither, Solar Energy Materials and Solar Cells. 92 (2008) 203–208. https://doi.org/10.1016/j.solmat.2006.10.027.
[9] F.G.K. Baucke, Electrochromic mirrors with variable reflectance, Solar Energy Materials. 16 (1987) 67–77. https://doi.org/10.1016/0165-1633(87)90009-8.
[10] K. Yamanaka, H. Oakamoto, H. Kidou, T. Kudo, Peroxotungstic Acid Coated Films for Electrochromic Display Devices, Jpn. J. Appl. Phys. 25 (1986) 1420. https://doi.org/10.1143/JJAP.25.1420.
[11] S. Li, Z. Yao, J. Zhou, R. Zhang, H. Shen, Fabrication and characterization of WO3 thin films on silicon surface by thermal evaporation, Materials Letters. 195 (2017) 213–216. https://doi.org/10.1016/j.matlet.2017.02.078.
[12] L.M. Bertus, A. Duta, Synthesis of WO3 thin films by surfactant mediated spray pyrolysis, Ceramics International. 38 (2012) 2873–2882. https://doi.org/10.1016/j.ceramint.2011.11.060.
[13] R. Godbole, S. Ameen, U.T. Nakate, M. Shaheer Akhtar, H.-S. Shin, Low temperature HFCVD synthesis of tungsten oxide thin film for high response hydrogen gas sensor application, Materials Letters. 254 (2019) 398–401. https://doi.org/10.1016/j.matlet.2019.07.110.
[14] S.V. Green, E. Pehlivan, C.G. Granqvist, G.A. Niklasson, Electrochromism in sputter deposited nickel-containing tungsten oxide films, Solar Energy Materials and Solar Cells. 99 (2012) 339–344. https://doi.org/10.1016/j.solmat.2011.12.025.
[15] X. Sun, Z. Liu, H. Cao, Effects of film density on electrochromic tungsten oxide thin films deposited by reactive dc-pulsed magnetron sputtering, Journal of Alloys and Compounds. 504 (2010) S418–S421. https://doi.org/10.1016/j.jallcom.2010.03.155.
[16] J. Yuan, B. Wang, H. Wang, Y. Chai, Y. Jin, H. Qi, J. Shao, Electrochromic behavior of WO3 thin films prepared by GLAD, Applied Surface Science. 447 (2018) 471–478. https://doi.org/10.1016/j.apsusc.2018.03.248.
[17] H. Yu, J. Guo, C. Wang, J. Zhang, J. Liu, G. Dong, X. Zhong, X. Diao, Essential role of oxygen vacancy in electrochromic performance and stability for WO3-y films induced by atmosphere annealing, Electrochimica Acta. 332 (2020) 135504. https://doi.org/10.1016/j.electacta.2019.135504.

[18] S.-H. Lee, H.M. Cheong, C.E. Tracy, A. Mascarenhas, A.W. Czanderna, S.K. Deb, Electrochromic coloration efficiency of a-WO3−y thin films as a function of oxygen deficiency, Appl. Phys. Lett. 75 (1999) 1541–1543. https://doi.org/10.1063/1.124782.
[19] B.-R. Koo, H.-J. Ahn, Fast-switching electrochromic properties of mesoporous WO3 films with oxygen vacancy defects, Nanoscale. 9 (2017) 17788–17793. https://doi.org/10.1039/C7NR06796H.
[20] W. Sahle, M. Nygren, Electrical conductivity and high resolution electron microscopy studies of WO3−x crystals with $0 \leq x \leq 0.28$, Journal of Solid State Chemistry. 48 (1983) 154–160. https://doi.org/10.1016/0022-4596(83)90070-1.
[21] L. Sang, B. Ren, T. Nabatame, M. Sumiya, M. Liao, Insight into traps at Al2O3/p-GaN metal-oxide-semiconductor interface fabricated on free-standing GaN substrate, Journal of Alloys and Compounds. 853 (2021) 157356. https://doi.org/10.1016/j.jallcom.2020.157356.
[22] J. Sánchez-González, A. Díaz-Parralejo, A.L. Ortiz, F. Guiberteau, Determination of optical properties in nanostructured thin films using the Swanepoel method, Applied Surface Science. 252 (2006) 6013–6017. https://doi.org/10.1016/j.apsusc.2005.11.009.
[23] R. Swanepoel, Determination of the thickness and optical constants of amorphous silicon, J. Phys. E: Sci. Instrum. 16 (1983) 1214–1222. https://doi.org/10.1088/0022-3735/16/12/023.
[24] K.B.J.-I. N'Djoré, M. Grafouté, Y. Makoudi, W. Hourani, C. Rousselot, Tuning the Electrical Properties of Tungsten Oxide Thin Films Deposited by Reactive Magnetron Sputtering, Coatings. 12 (2022) 274. https://doi.org/10.3390/coatings12020274.
[25] C. Liu, Y.-M. Zhang, Y.-M. Zhang, H.-L. Lü, Interfacial characteristics of Al/Al2O3/ZnO/n-GaAs MOS capacitor, Chinese Phys. B. 22 (2013) 076701. https://doi.org/10.1088/1674-1056/22/7/076701.
[26] L.M. Terman, An investigation of surface states at a silicon/silicon oxide interface employing metal-oxide-silicon diodes, Solid-State Electronics. 5 (1962) 285–299. https://doi.org/10.1016/0038-1101(62)90111-9.
[27] B. Wen-Cheun Au, K.-Y. Chan, D. Knipp, Effect of film thickness on electrochromic performance of sol-gel deposited tungsten oxide (WO3), Optical Materials. 94 (2019) 387–392. https://doi.org/10.1016/j.optmat.2019.05.051.
[28] S. Deb, Opportunities and challenges in science and technology of WO 3 for electrochromic and related applications, Solar Energy Materials and Solar Cells. 92 (2008) 245–258. https://doi.org/10.1016/j.solmat.2007.01.026.
[29] C. Li, J.H. Hsieh, M.-T. Hung, B.Q. Huang, Electrochromic study on amorphous tungsten oxide films by sputtering, Thin Solid Films. 587 (2015) 75–82. https://doi.org/10.1016/j.tsf.2014.12.022.
[30] B. Balland, Optique géométrique: imagerie et instruments, PPUR presses polytechniques, 2007.
[31] V. Madhavi, P. Kondaiah, O.M. Hussain, S. Uthanna, Structural, optical and electrochromic properties of RF magnetron sputtered WO3 thin films, Physica B: Condensed Matter. 454 (2014) 141–147. https://doi.org/10.1016/j.physb.2014.07.029.
[32] E. Washizu, A. Yamamoto, Y. Abe, M. Kawamura, K. Sasaki, Optical and electrochromic properties of RF reactively sputtered WO3 films, Solid State Ionics. 165 (2003) 175–180. https://doi.org/10.1016/j.ssi.2003.08.030.
[33] S. Sawada, G.C. Danielson, Optical Indices of Refraction of WO3, Phys. Rev. 113 (1959) 1008–1013. https://doi.org/10.1103/PhysRev.113.1008.
[34] C. Charles, N. Martin, M. Devel, J. Ollitrault, A. Billard, Correlation between structural and optical properties of WO3 thin films sputter deposited by glancing angle deposition, Thin Solid Films. 534 (2013) 275–281. https://doi.org/10.1016/j.tsf.2013.03.004.
[35] K.M. Sobahan, Y. Park, C.K. Hwangbo, Effect of Deposition Angle on the Optical and the StructuralProperties of Ta_2O_5 Thin Films Fabricated by Using GlancingAngle

Deposition, Journal of The Korean Physical Society - J KOREAN PHYS SOC. 55 (2009). https://doi.org/10.3938/jkps.55.1272.
[36] K.M. Sobahan, Y. Park, C. Hwangbo, Optical and Structural Properties of ZrO2 Thin FilmsFabricated by Using Glancing Angle Deposition, Journal of the Korean Physical Society. 53 (2008) 2544–2548. https://doi.org/10.3938/jkps.53.2544.
[37] B.-R. Koo, H.-J. Ahn, Fast-switching electrochromic properties of mesoporous WO3 films with oxygen vacancy defects, Nanoscale. 9 (2017) 17788–17793. https://doi.org/10.1039/C7NR06796H.
[38] C. Guillén, J. Herrero, Amorphous WO3-x thin films with color characteristics tuned by the oxygen vacancies created during reactive DC sputtering, Journal of Materials Science & Technology. 78 (2021) 223–228. https://doi.org/10.1016/j.jmst.2020.11.036.
[39] J.V. Gabrusenoks, P.D. Cikmach, A.R. Lusis, J.J. Kleperis, G.M. Ramans, Electrochromic colour centres in amorphous tungsten trioxide thin films, Solid State Ionics. 14 (1984) 25–30. https://doi.org/10.1016/0167-2738(84)90006-7.
[40] S.S. Chan, I.E. Wachs, L.L. Murrell, N.C. Dispenziere, Laser Raman characterization of tungsten oxide supported on alumina: Influence of calcination temperatures, Journal of Catalysis. 92 (1985) 1–10. https://doi.org/10.1016/0021-9517(85)90231-3.
[41] Y. Shigesato, A. Murayama, T. Kamimori, K. Matsuhiro, Characterization of evaporated amorphous WO3 films by Raman and FTIR spectroscopies, Applied Surface Science. 33–34 (1988) 804–811. https://doi.org/10.1016/0169-4332(88)90384-4.
[42] E. Salje, Lattice dynamics of WO3, Acta Cryst A. 31 (1975) 360–363. https://doi.org/10.1107/S0567739475000757.
[43] M.F. Daniel, B. Desbat, J.C. Lassegues, B. Gerand, M. Figlarz, Infrared and Raman study of WO3 tungsten trioxides and WO3, xH2O tungsten trioxide tydrates, Journal of Solid State Chemistry. 67 (1987) 235–247. https://doi.org/10.1016/0022-4596(87)90359-8.
[44] J. Pfeifer, C. Guifang, P. Tekula-Buxbaum, B.A. Kiss, M. Farkas-Jahnke, K. Vadasdi, A reinvestigation of the preparation of tungsten oxide hydrate WO3, 1/3H2O, Journal of Solid State Chemistry. 119 (1995) 90–97. https://doi.org/10.1016/0022-4596(95)80013-F.
[45] S.-H. Lee, H.M. Cheong, C.E. Tracy, A. Mascarenhas, D.K. Benson, S.K. Deb, Raman spectroscopic studies of electrochromic a-WO3, Electrochimica Acta. 44 (1999) 3111–3115. https://doi.org/10.1016/S0013-4686(99)00027-4.
[46] S. Lee, H. Cheong, J.-G. Zhang, A. Mascarenhas, D. Benson, S.K. Deb, Electrochromic mechanism in a-WO3−y thin films, (1999). https://doi.org/10.1063/1.123268.
[47] S.-H. Lee, H.M. Cheong, P. Liu, D. Smith, C.E. Tracy, A. Mascanrenhas, J.R. Pitts, S.K. Deb, Gasochromic mechanism in a-WO3 thin films based on Raman spectroscopic studies, Journal of Applied Physics. 88 (2000) 3076–3078. https://doi.org/10.1063/1.1287407.
[48] Y. Huang, Y. Zhang, X.T. Zeng, X. Hu, Study on Raman spectra of electrochromic C-WO3 films and their infrared emittance modulation characteristics, Applied Surface Science. 202 (2002) 104–109. https://doi.org/10.1016/S0169-4332(02)00943-1.
[49] S.-H. Lee, H.M. Cheong, P. Liu, D. Smith, C.E. Tracy, A. Mascarenhas, J. Roland Pitts, S.K. Deb, Raman spectroscopic studies of gasochromic a-WO3 thin films, Electrochimica Acta. 46 (2001) 1995–1999. https://doi.org/10.1016/S0013-4686(01)00379-6.
[50] R.F. Garcia-Sanchez, T. Ahmido, D. Casimir, S. Baliga, P. Misra, Thermal Effects Associated with the Raman Spectroscopy of WO3 Gas-Sensor Materials, J. Phys. Chem. A. 117 (2013) 13825–13831. https://doi.org/10.1021/jp408303p.
[51] A. Chemseddine, M. Henry, J. Livage, Rev. Chim. Miner. 21, 487., (1984).
[52] C. Santato, M. Odziemkowski, M. Ulmann, J. Augustynski, Crystallographically Oriented Mesoporous WO3 Films: Synthesis, Characterization, and Applications, J. Am. Chem. Soc. 123 (2001) 10639–10649. https://doi.org/10.1021/ja011315x.
[53] G.L. Frey, A. Rothschild, J. Sloan, R. Rosentsveig, R. Popovitz-Biro, R. Tenne, Investigations of Nonstoichiometric Tungsten Oxide Nanoparticles, Journal of Solid State Chemistry. 162 (2001) 300–314. https://doi.org/10.1006/jssc.2001.9319.

[54] Y.-R. Ma, C.-M. Lin, C.-L. Yeh, R.-T. Huang, Synthesis and characterization of one-dimensional WO2 nanorods, Journal of Vacuum Science & Technology B: Microelectronics and Nanometer Structures Processing, Measurement, and Phenomena. 23 (2005) 2141–2145. https://doi.org/10.1116/1.2050668.
[55] E.A. Tutov, MOS structures with amorphous tungsten trioxide for capacitive humidity sensors, Semiconductors. 42 (2008) 1561–1563. https://doi.org/10.1134/S106378260813023X.
[56] B.J. Gordon, C-V plotting: myths and methods, Solid State Technology. 36 (1993) 57–62.
[57] Y. Maneglia, D. Bauza, Extraction of slow oxide trap concentration profiles in metal–oxide–semiconductor transistors using the charge pumping method, Journal of Applied Physics. 79 (1996) 4187–4192. https://doi.org/10.1063/1.361786.
[58] D. Bauza, G. Ghibaudo, Analytical study of the contribution of fast and slow oxide traps to the charge pumping current in MOS structures, Solid-State Electronics. 39 (1996) 563–570. https://doi.org/10.1016/0038-1101(95)00156-5.
[59] E. Atanassova, D. Spassov, A. Paskaleva, Influence of the metal electrode on the characteristics of thermal Ta2O5 capacitors, Microelectronic Engineering. 83 (2006) 1918–1926. https://doi.org/10.1016/j.mee.2006.01.043.
[60] Schroder, D.K. Semiconductor Material and Device Characterization, 3rd ed.; John Wiley & Sons, Inc.: Hoboken, NJ, USA, (2006).
[61] Y. Yue, Y. Hao, Q. Feng, J. Zhang, X. Ma, J. Ni, Study of GaN MOS-HEMT using ultrathin Al2O3 dielectric grown by atomic layer deposition, Sci. China Ser. E-Technol. Sci. 52 (2009) 2762–2766. https://doi.org/10.1007/s11431-008-0231-5.
[62] M. Hutchins, N. Kamel, K. Abdel-Hady, Effect of oxygen content on the electrochromic properties of sputtered tungsten oxide films with Li+ insertion, Vacuum. 51 (1998) 433–439. https://doi.org/10.1016/S0042-207X(98)00189-4.
[63] C. Brigouleix, P. Topart, E. Bruneton, F. Sabary, G. Nouhaut, G. Campet, Roll-to-roll pulsed dc magnetron sputtering deposition of WO3 for electrochromic windows, Electrochimica Acta. 46 (2001) 1931–1936. https://doi.org/10.1016/S0013-4686(01)00362-0.
[64] A.I. Inamdar, Y.S. Kim, B.U. Jang, H. Im, W. Jung, D.-Y. Kim, H. Kim, Effects of oxygen stoichiometry on electrochromic properties in amorphous tungsten oxide films, Thin Solid Films. 520 (2012) 5367–5371. https://doi.org/10.1016/j.tsf.2012.04.026.
[65] T.J. Vink, E.P. Boonekamp, R.G.F.A. Verbeek, Y. Tamminga, Lithium trapping at excess oxygen in sputter-deposited a-WO3 films, Journal of Applied Physics. 85 (1999) 1540–1544. https://doi.org/10.1063/1.369284.
[66] Y. Yao, Q. Zhao, W. Wei, Z. Chen, Y. Zhu, P. Zhang, Z. Zhang, Y. Gao, WO3 quantum-dots electrochromism, Nano Energy. 68 (2020) 104350. https://doi.org/10.1016/j.nanoen.2019.104350.
[67] P. Limnonthakul, W. Luangtip, C. Puttharugsa, I. Lutchanont, C. Chananonnawathorn, P. Eiamchai, S. Limwichean, V. Pattantsetakul, M. Horprathum, Influence of oxygen flow rate on electrochromic property of WO3 nanorods prepared by glancing reactive magnetron sputtering, Materials Today: Proceedings. 4 (2017) 6218–6223. https://doi.org/10.1016/j.matpr.2017.06.119.
[68] L.-C. Chen, K.-C. Ho, Design equations for complementary electrochromic devices: application to the tungsten oxide–Prussian blue system, Electrochimica Acta. 46 (2001) 2151–2158. https://doi.org/10.1016/S0013-4686(01)00368-1.
[69] C.G. Granqvist, S. Green, G.A. Niklasson, N.R. Mlyuka, S. von Kræmer, P. Georén, Advances in chromogenic materials and devices, Thin Solid Films. 518 (2010) 3046–3053. https://doi.org/10.1016/j.tsf.2009.08.058.
[70] H.T.D. Nguyen, D. Zhang, T.M. Nguyen, H. Zhang, J. Seidel, Topotactic Electrochromism for Efficient Coloration Applications, Advanced Optical Materials. 9 (2021) 2100955. https://doi.org/10.1002/adom.202100955.

Tables list

Q (O_2) (sccm)	Total pressure (Pa) ± 0.01Pa	Films thickness (nm) ± 15 nm	EDS ratio (at. % O /at. % W)
1.20	0.45	589	1.92
1.65	0.53	582	2.56
1.95	0.61	565	-
3.00	0.83	507	2.70
4.50	1.13	500	2.85
6.00	1.37	502	2.92
8.00	1.70	528	2.94
14.00	2.60	487	3.00

Table 1: Thicknesses and EDS ratio of WO_x thin films deposited onto glass with various oxygen flow rates and total pressures. The relative error on EDS ratio is 3%.

Attribution	$Q(O_2)$ (sccm)			Attribution
	14 → 1.95	1.65	1.20	
O-W^{6+}-O bending [43]	278 (140)	221 (93)		W^{4+}-O [45]
		268 (35)		W^{4+}-O
		320 (114)		O-W^{5+}-O [45]
		423 (71)		W^{5+}=O [45]
		458 (26)		
O-W^{6+}-O stretching [39,43]	671 (122) 782 (153)	671 (122) 782 (153)		O-W^{6+}-O stretching [39,43]
		922 (145)	885 (115)	stretching
W^{6+}=O stretching [39]	961 (95) 1015 (20)	961 (95) 1015 (20)		W^{6+}=O stretching [39]

Table 2 : Wavenumbers and Full Width at Half Maximum (in parenthesis), cm^{-1}, of the bands deduced from the refinements (gaussian profile) of the Raman spectra of samples deposited with $Q(O_2) \geq 1.95$ sccm, $Q(O_2)$ =1.65 sccm, and $Q(O_2) = 1.20$ sccm.

Q (O_2) (sccm)	Hysteresis ΔV (V) $\pm$ 2 %	$D_{it\text{-}average}$ * 10^{12} states/cm^2/eV ± 7.5 %	Ions density*10^{12} N_{ss} (ions/cm^2) ± 7.6 %	Oxide capacitance * 10^{10} (Farad) ± 1.2 %
1.20	0.003	1.1	0.9	8,88
1.65	1.43	4.5	11.2	6,06
1.95	1.80	16.4	14.2	5,75
3.00	2.80	35.7	12.4	5,52
4.50	2.00	24.4	10.7	5,45
6.00	1.72	9.2	4.1	6,07
8.00	2.00	3.9	1.1	5,36
14.00	1.70	5.3	-1.8	4,01

Table 3: Oxygen flow rates with the various corresponding defects identified in the film by the measurements of the electrical parameters $\boldsymbol{\Delta}$V, D_{it}, N_{ss} and C_{ox}. The relative errors on the hysteresis mid-height width, interface traps average distribution, ions density and oxide capacitance are 2 %, 7.5 %, 7.6 % and 1.2 %, respectively.

Q O_2 (sccm)	$t_{coloration}$ (s)	$t_{discoloration}$ (s)
4.5	19	180
6	22	75
8	30	9
14	27	8

Table 4: Response time for WO_x films.

Figures caption

Figure 1: (a) Effect of oxygen flow rate on optical transmittance spectra as a function of the wavelength of WO_x films deposited on glass substrate. (b) Evolution of average optical transmittance in the visible region as a function of oxygen flow rate. In insert, XRD patterns of a-WOx films deposited on glass for $Q(O_2)$ = 1.2, 4.5 and 14 sccm.

Figure 2: Influence of oxygen flow rate increase and total pressure increase on the evolution of WO_x thin films refractive index as a function of the wavelength in visible region.

Figure 3: Evolution of average refractive index between $425\ nm \leq \lambda \leq 800\ nm$. and average porosity of transparent WO_x thin films as a function total pressure and oxygen flow rate.

Figure 4: SEM observations were performed on cross sections of the films deposited on silicon substrates with oxygen flow rates of 1.2 sccm ($WO_{1.92}$), 4.5 sccm ($WO_{2.85}$) and 14 sccm (WO_3).

Figure 5: Raman spectra of selected samples deposited with $Q(O_2)$ = 14.00, 1.95 and 1.20 sccm (accumulation time 1200 s, 10 accumulations), and Raman spectrum of crystallized WO_3 (monoclinic) collected in the same spectral range (accumulation time 120 s, 2 accumulations). The single stars (*) stands for contamination by very narrow plasma lines. The double stars (**) indicate contamination by the set of narrow Raman lines of air (rotational lines) in the near vicinity of the surface of the samples. The dotted lines define the low and high frequency ranges selected for the refinements, as already considered [39,43].

Figure 6: Raman spectra of samples deposited with $Q(O_2)$ = 1.95, 1.65, and 1.20 sccm with their fitted curves (colored lines) obtained by least squares method. Each spectrum is

deconvoluted by the sum of gaussian shape bands. Stars (*) at 235 cm^{-1} stands for contamination by plasma line.

Figure 7: Integrate intensity ratio as a function of $Q(O_2)$ (a), and as a function of the EDS O/W ratio (b), with respect to the O-W^{6+}-O stretching band at 671-782 cm^{-1}, of the band at 278 cm^{-1} attributed to O-W^{6+}-O bending (square), and the band at 961 cm^{-1} attributed to W^{6+}=O stretching (dot). The dotted lines are just guides for the eye.

Figure 8: Integrate intensity ratio as a function of $Q(O_2)$ (a), and as a function of the EDS O/W ratio (b), with respect to the O-W^{6+}-O band at 671-782 cm^{-1}, of the lines attributed to W^{6+} at 278 cm^{-1} (square), O-W^{5+}-O at 320 cm^{-1} (blue dot), W^{5+}=O at 423, and 458 cm^{-1} (green dot), W^{4+} at 221 cm^{-1} (triangle), and of the narrow line at 268 cm (red diamond). The dotted lines are just guide for the eye.

Figure 9: Hysteresis loop of the WO_x film deposited with Q (O_2) = 8 sccm

Figure 10: Cyclic voltammograms of WO_x films deposited with various oxygen flow rates. The 1^{rst} and the 5^{th} CV curves are shown for each film. The scanning speed is 20 mV / s.

Figure 11: Evolution of the current density vs time during coloration (a) and discoloration (b).

Figure 12: Optical transmittance of as deposited, bleached and colored WO_x thin films and optical modulation at 632 nm. The dash lines for bleached states represent the initial optical transmittance of the as deposited a-WO_x films.

Figure 13: Coloration efficiency versus wavelength for films deposited with variable oxygen flow rate.

Figure 14: Evolution of electrical parameters and coloration efficiency at 632 nm as a function of oxygen flow rate.

List of Figures

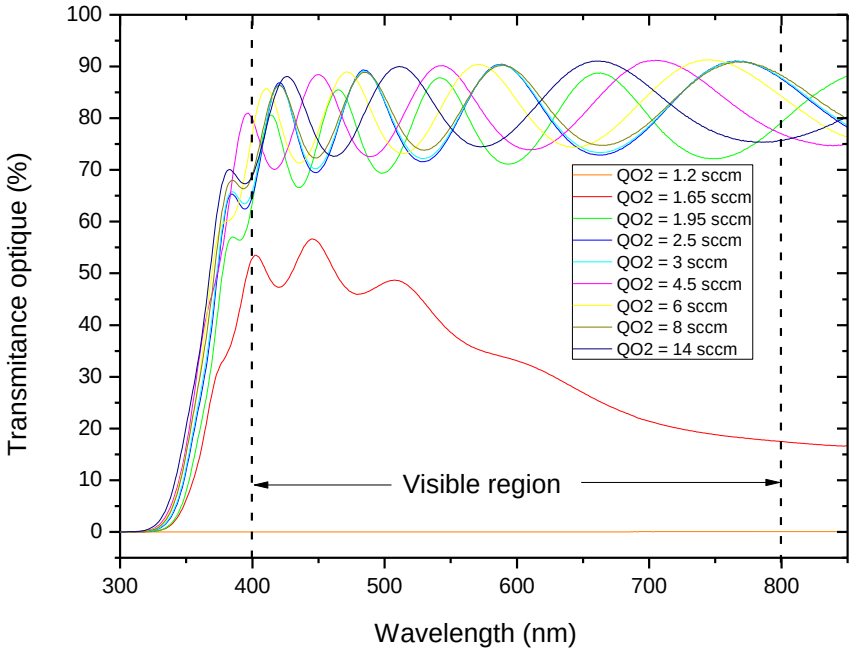

1 a

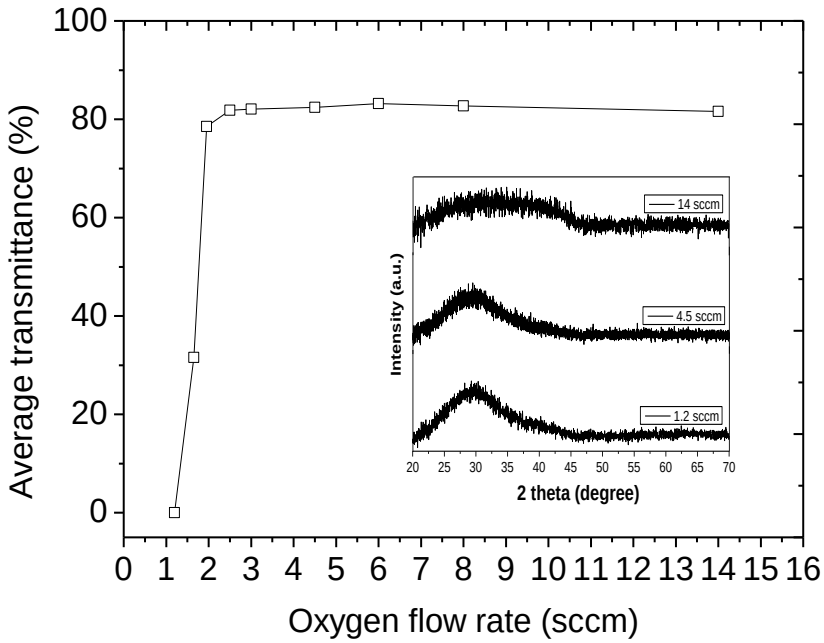

1 b

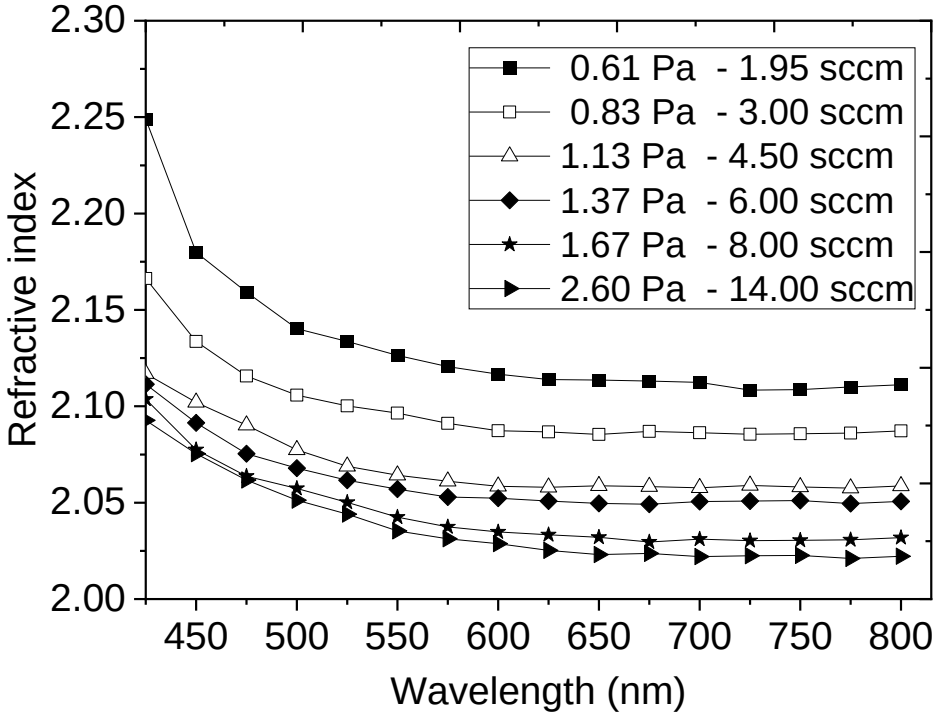
Refractive index
Wavelength (nm)
0.61 Pa - 1.95 sccm
0.83 Pa - 3.00 sccm
1.13 Pa - 4.50 sccm
1.37 Pa - 6.00 sccm
1.67 Pa - 8.00 sccm
2.60 Pa - 14.00 sccm
2.30
2.25
2.20
2.15
2.10
2.05
2.00
450
500
550
600
650
700
750
800

2

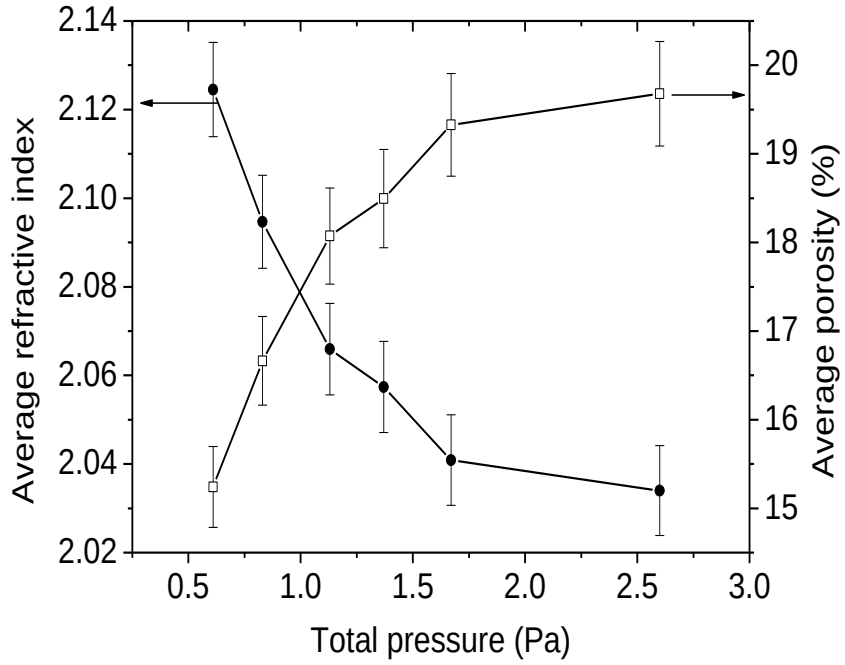
Average refractive index
Average porosity (%)
Total pressure (Pa)
2.14
2.12
2.10
2.08
2.06
2.04
2.02
20
19
18
17
16
15
0.5
1.0
1.5
2.0
2.5
3.0

3

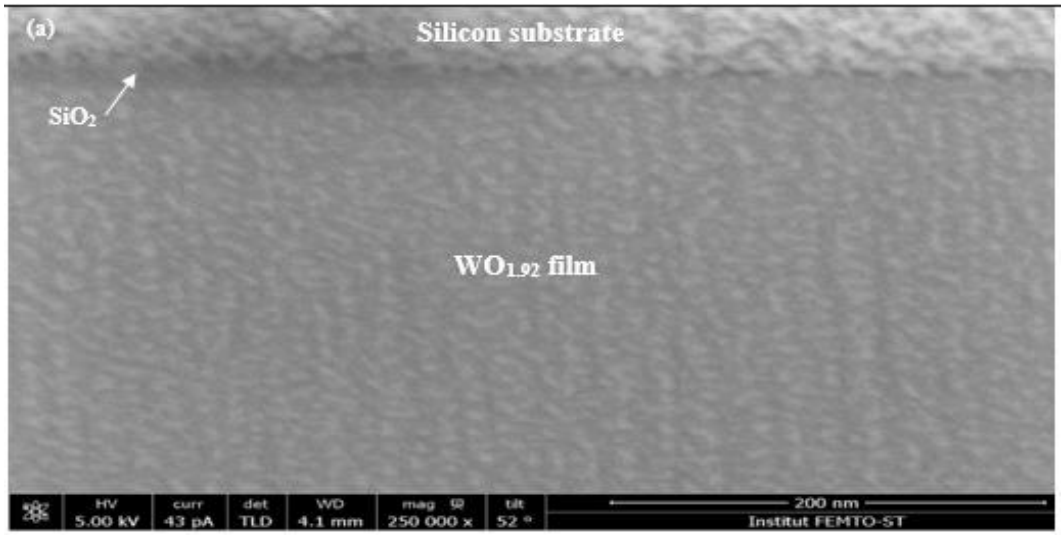
(a)
Silicon substrate
SiO2
WO1.92 film
HV
5.00 kV
curr
43 pA
det
TLD
WD
4.1 mm
mag
250 000 x
tilt
52 °
200 nm
Institut FEMTO-ST

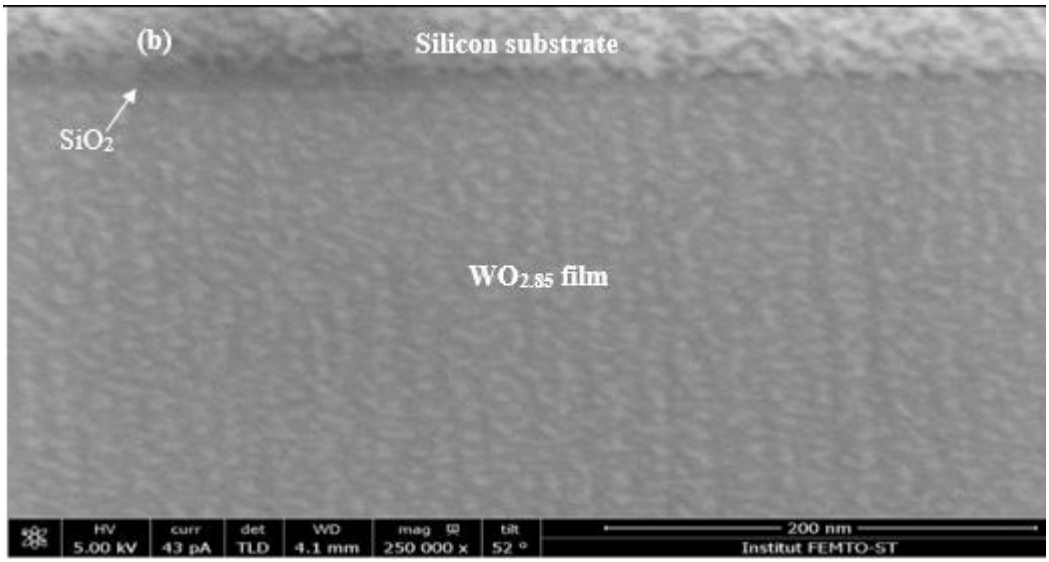
(b)
Silicon substrate
SiO2
WO2.85 film
HV
5.00 kV
curr
43 pA
det
TLD
WD
4.1 mm
mag
250 000 x
tilt
52 °
200 nm
Institut FEMTO-ST

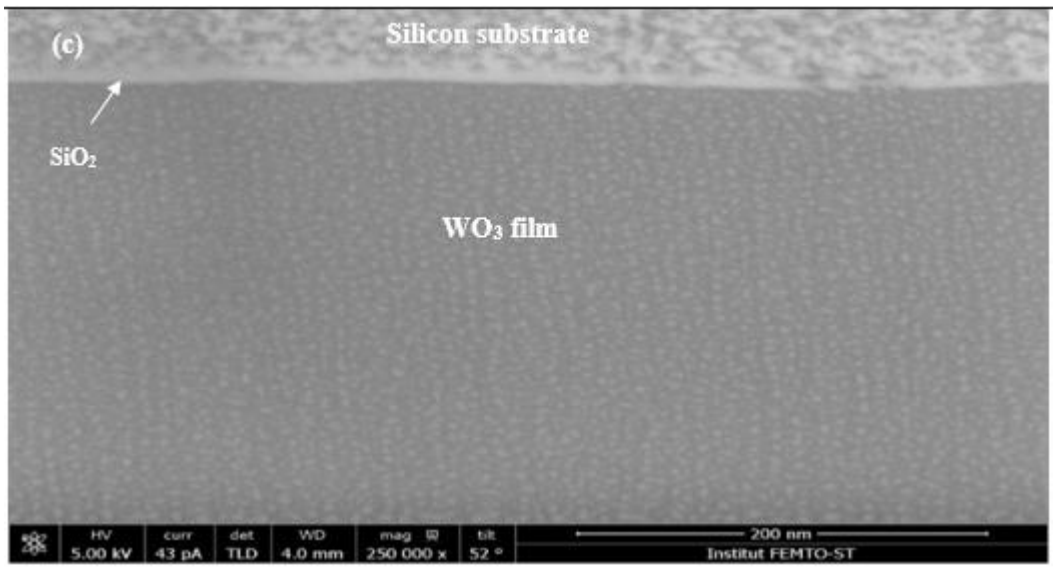
(c)
Silicon substrate
SiO2
WO3 film
HV
5.00 kV
curr
43 pA
det
TLD
WD
4.0 mm
mag
250 000 x
tilt
52 °
200 nm
Institut FEMTO-ST

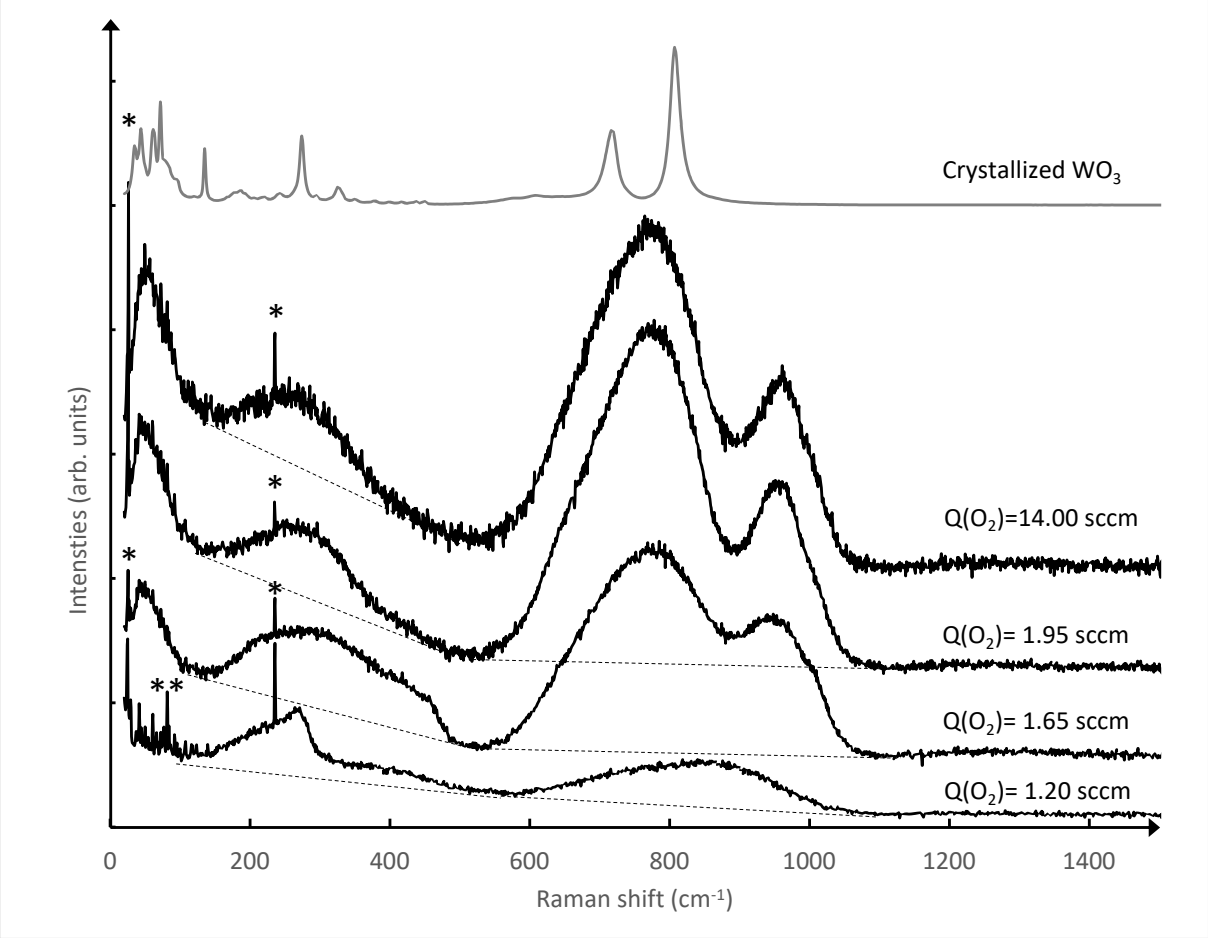
Crystallized WO3
Q(O2)=14.00 sccm
Q(O2)= 1.95 sccm
Q(O2)= 1.65 sccm
Q(O2)= 1.20 sccm
Intensties (arb. units)
Raman shift (cm-1)
0
200
400
600
800
1000
1200
1400

5

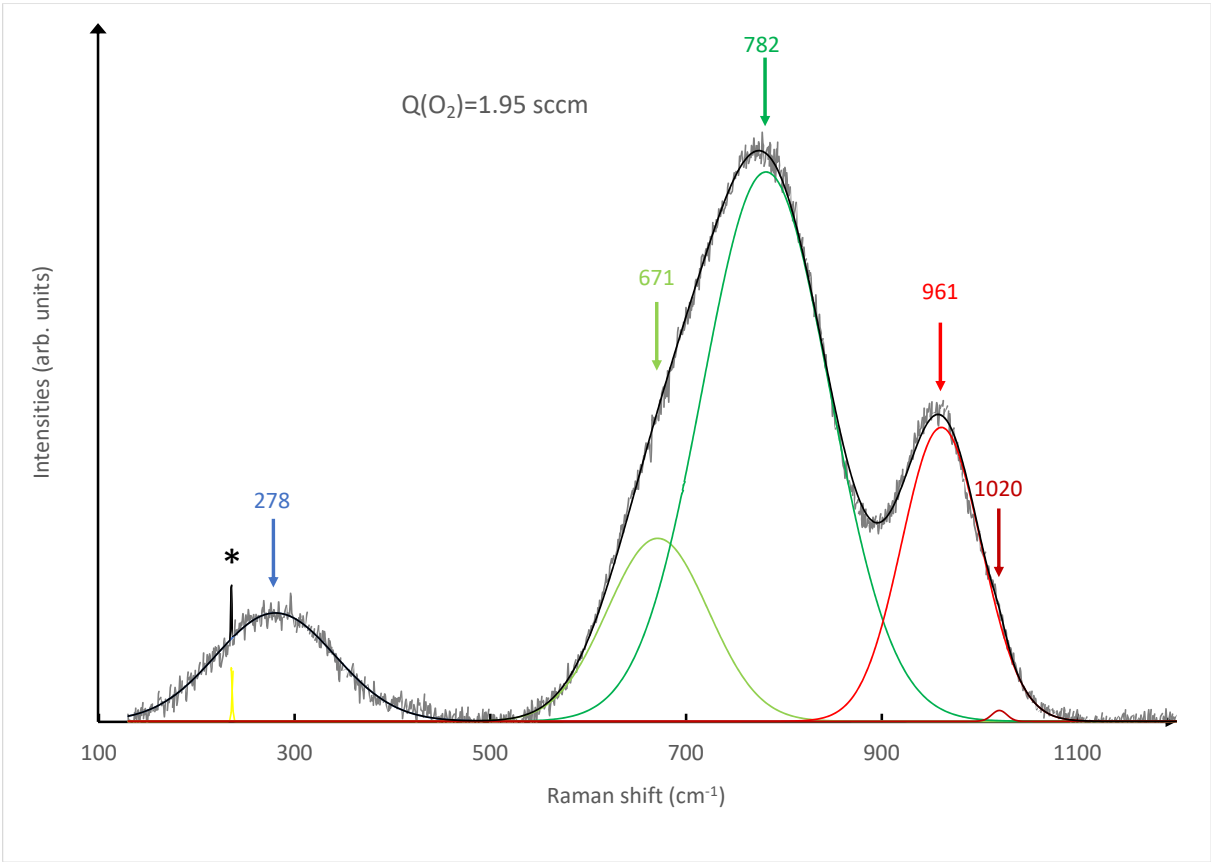
Q(O2)=1.95 sccm
782
671
961
1020
278
*
Intensities (arb. units)
100
300
500
700
900
1100
Raman shift (cm-1)

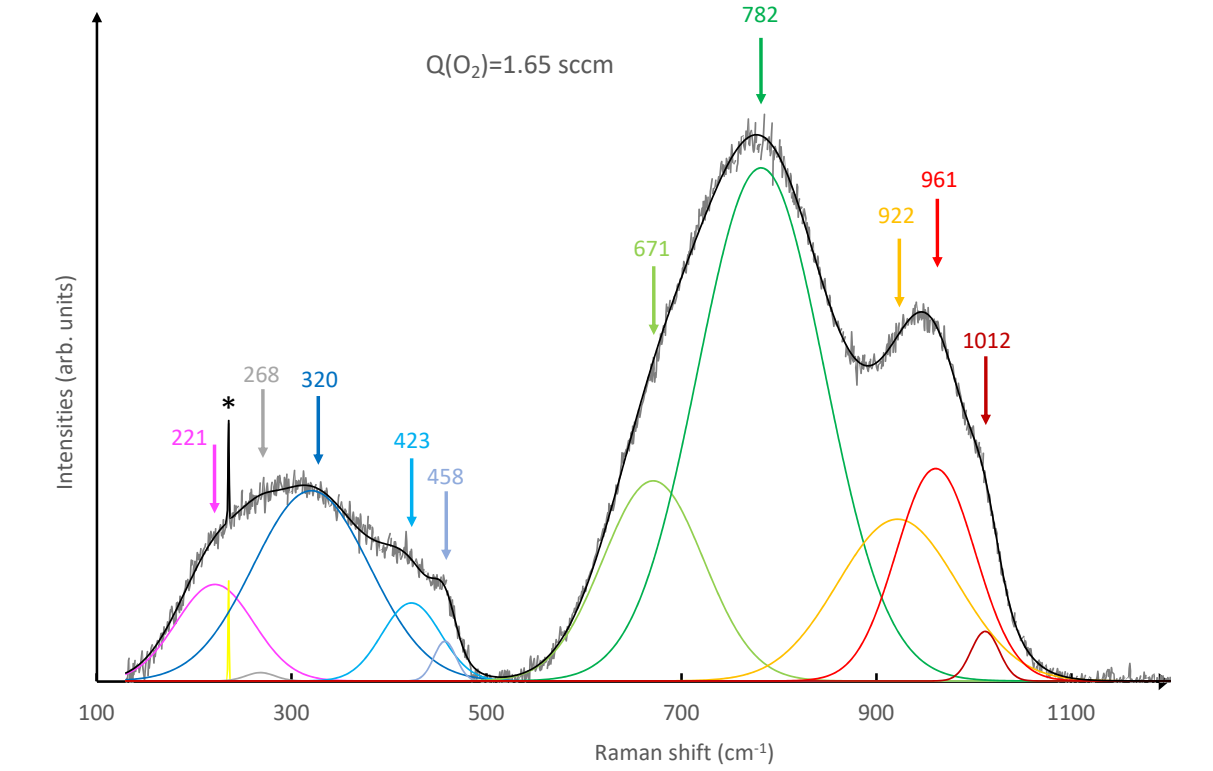
Q(O2)=1.65 sccm
782
961
922
671
1012
268
320
*
221
423
458
Intensities (arb. units)
100
300
500
700
900
1100
Raman shift (cm-1)

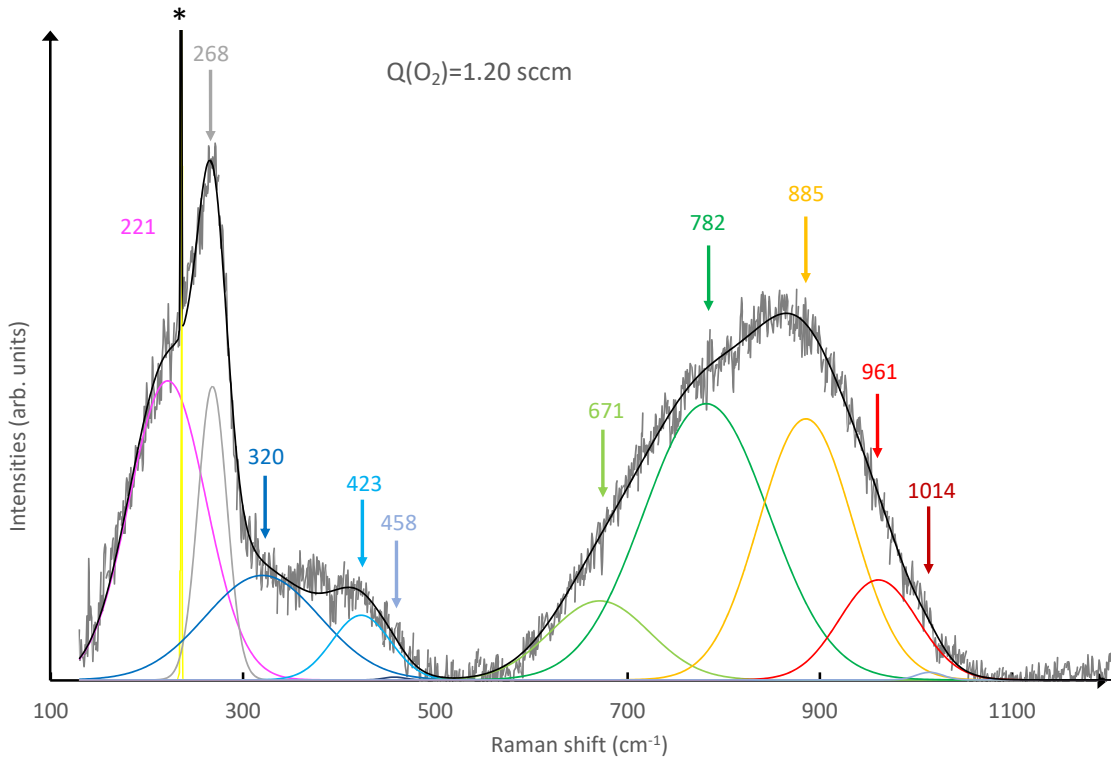
*
268
Q(O2)=1.20 sccm
221
885
782
961
671
320
423
458
1014
Intensities (arb. units)
100
300
500
700
900
1100
Raman shift (cm-1)

6

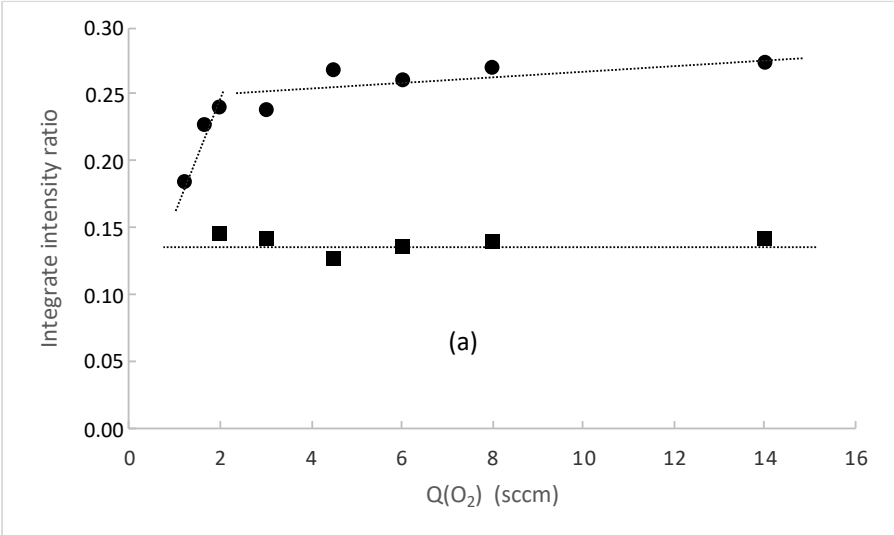
0.30
0.25
0.20
0.15
0.10
0.05
0.00
Integrate intensity ratio
(a)
0
2
4
6
8
10
12
14
16
Q(O2) (sccm)

7 a

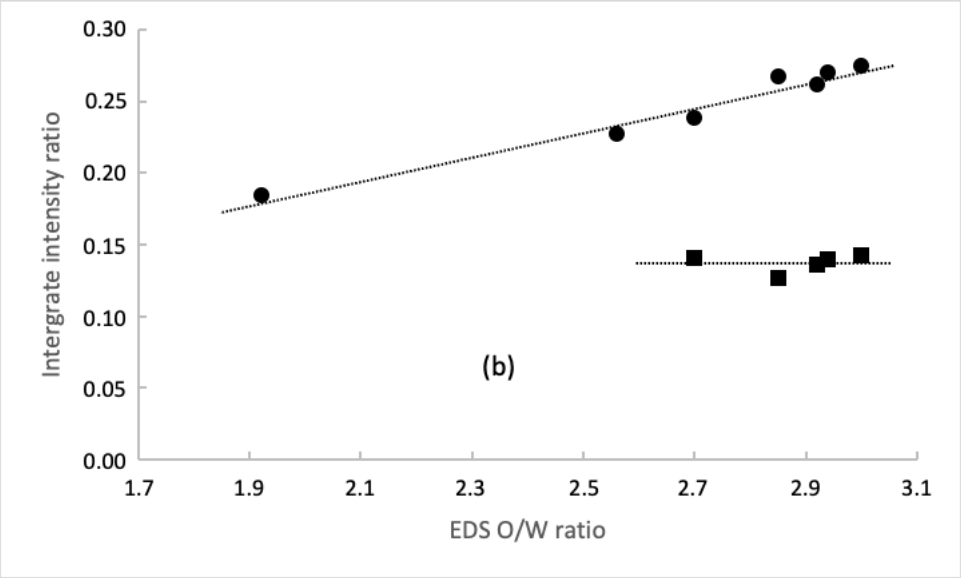
Intergrate intensity ratio
0.30
0.25
0.20
0.15
0.10
0.05
0.00
1.7
1.9
2.1
2.3
2.5
2.7
2.9
3.1
EDS O/W ratio
(b)

7 b

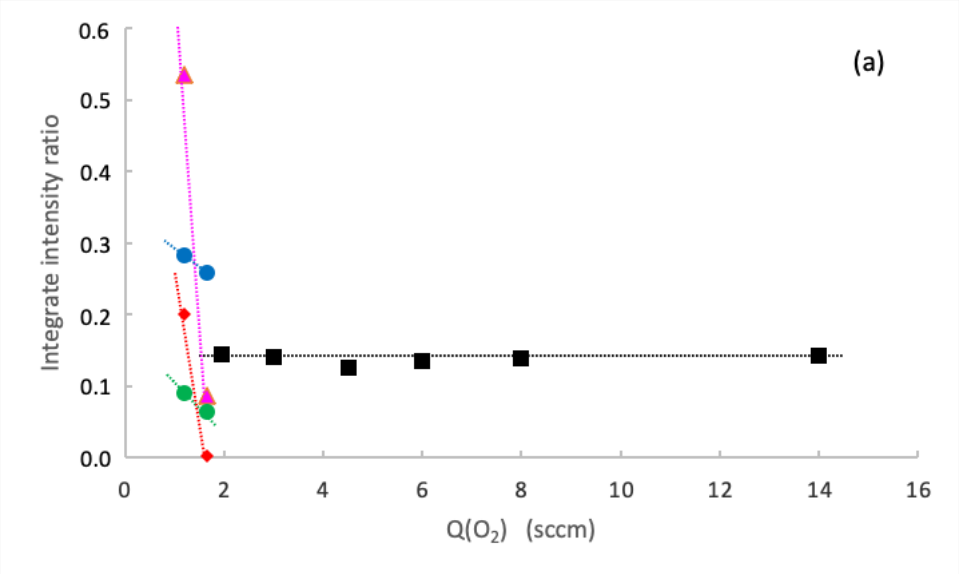
Integrate intensity ratio
0.6
0.5
0.4
0.3
0.2
0.1
0.0
0
2
4
6
8
10
12
14
16
Q(O2) (sccm)
(a)

8 a

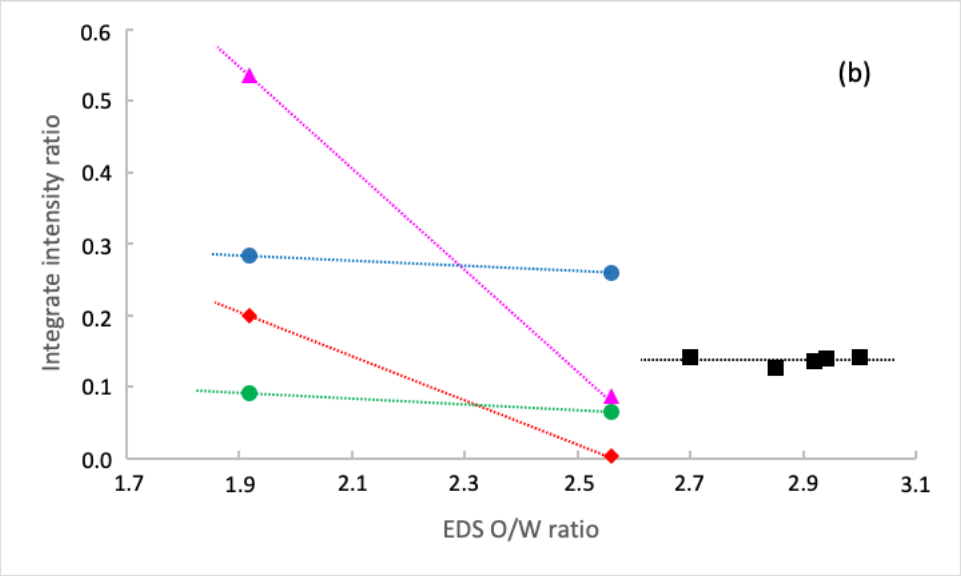
(b)
Integrate intensity ratio
0.6
0.5
0.4
0.3
0.2
0.1
0.0
1.7
1.9
2.1
2.3
2.5
2.7
2.9
3.1
EDS O/W ratio

8 b

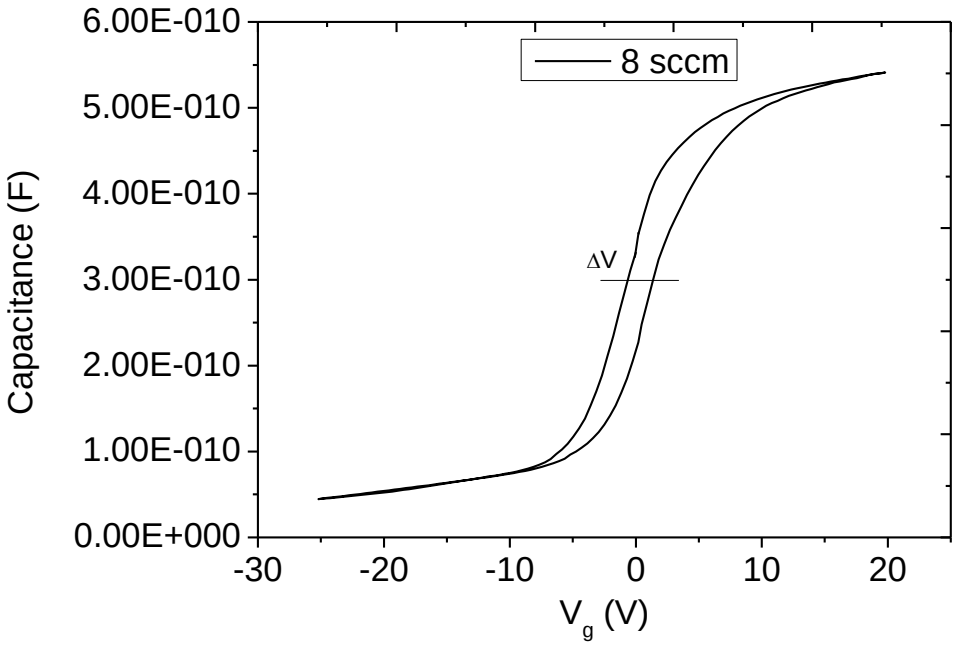
8 sccm
ΔV
Capacitance (F)
6.00E-010
5.00E-010
4.00E-010
3.00E-010
2.00E-010
1.00E-010
0.00E+000
-30
-20
-10
0
10
20
V_g (V)

9

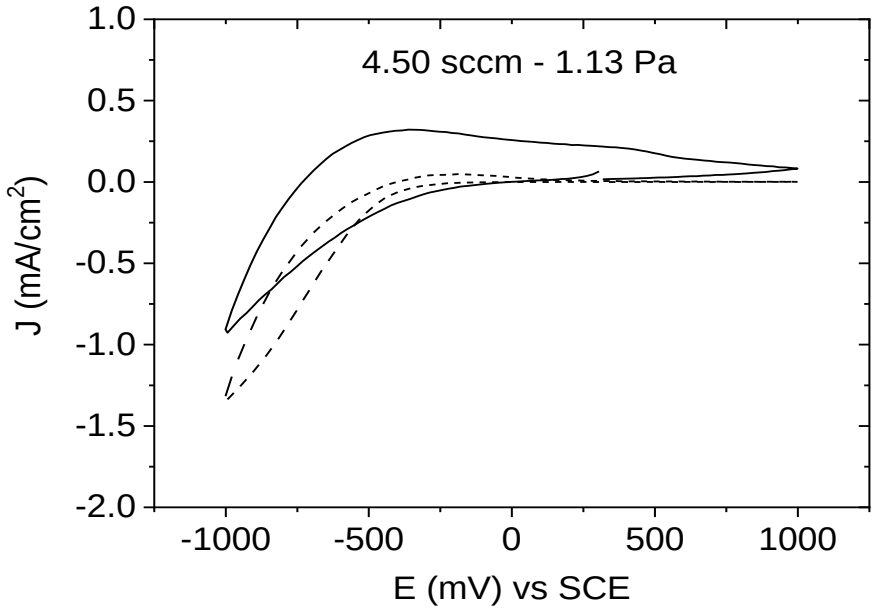
4.50 sccm - 1.13 Pa
J (mA/cm2)
E (mV) vs SCE
1.0
0.5
0.0
-0.5
-1.0
-1.5
-2.0
-1000
-500
0
500
1000

10 a

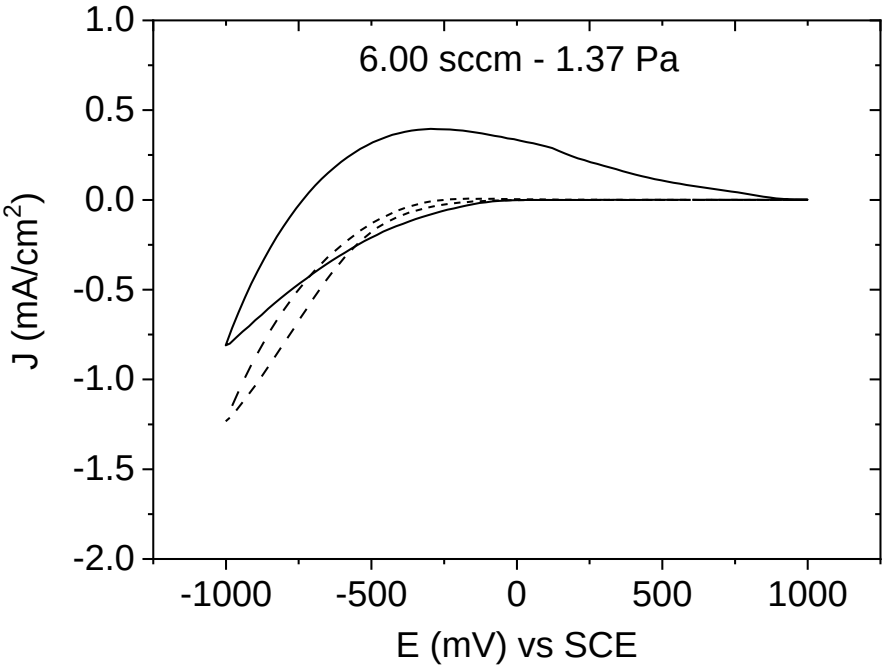
6.00 sccm - 1.37 Pa
J (mA/cm2)
E (mV) vs SCE
1.0
0.5
0.0
-0.5
-1.0
-1.5
-2.0
-1000
-500
0
500
1000

10 b

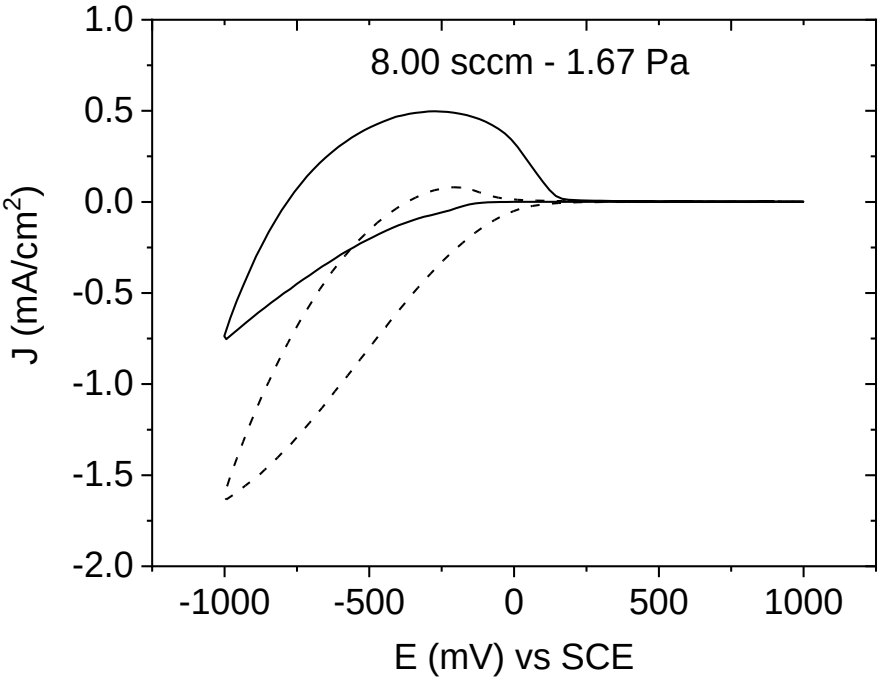
8.00 sccm - 1.67 Pa
J (mA/cm2)
E (mV) vs SCE
1.0
0.5
0.0
-0.5
-1.0
-1.5
-2.0
-1000
-500
0
500
1000

10 c

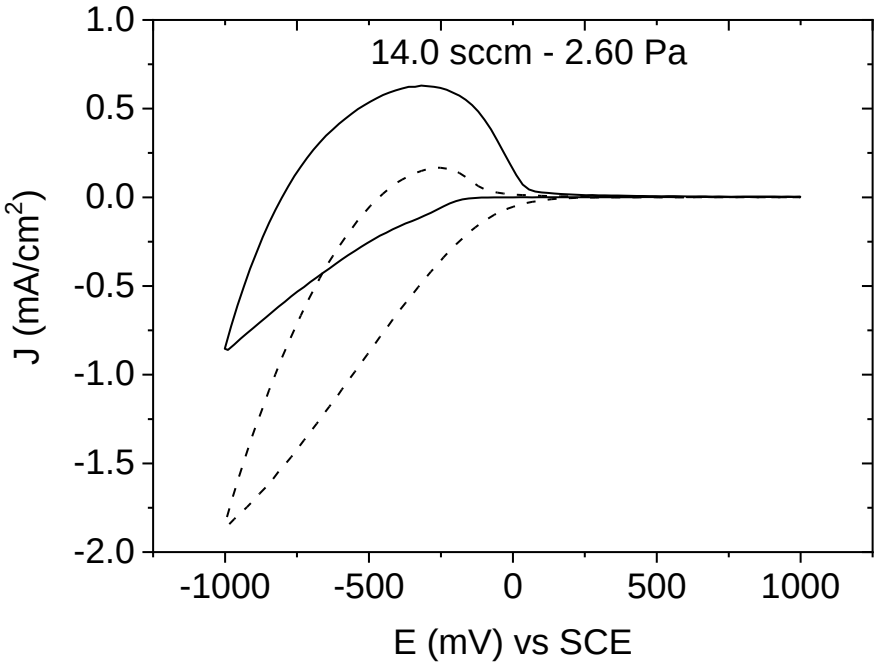
14.0 sccm - 2.60 Pa
J (mA/cm2)
E (mV) vs SCE
1.0
0.5
0.0
-0.5
-1.0
-1.5
-2.0
-1000
-500
0
500
1000

10 d

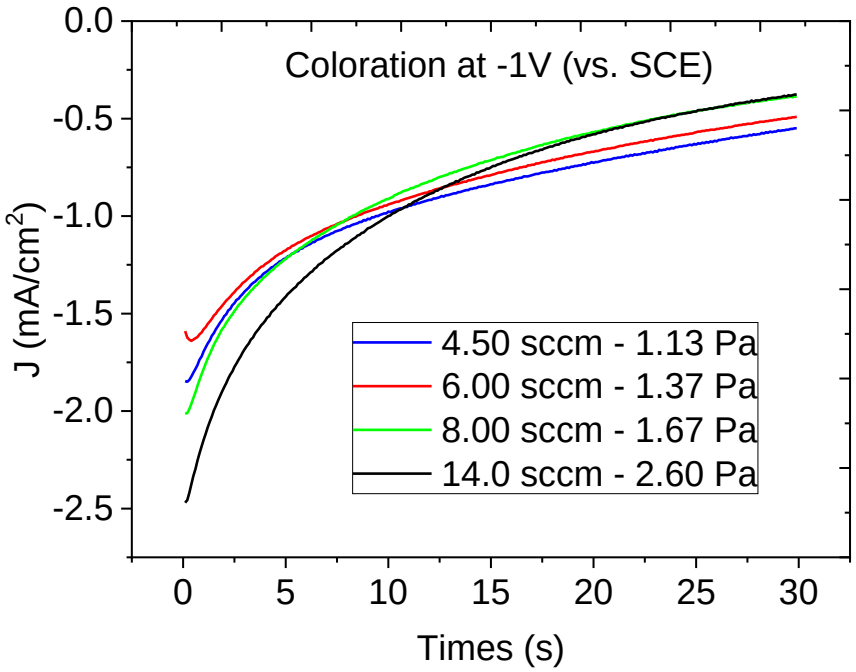
Coloration at -1V (vs. SCE)
J (mA/cm2)
Times (s)
4.50 sccm - 1.13 Pa
6.00 sccm - 1.37 Pa
8.00 sccm - 1.67 Pa
14.0 sccm - 2.60 Pa

11 a

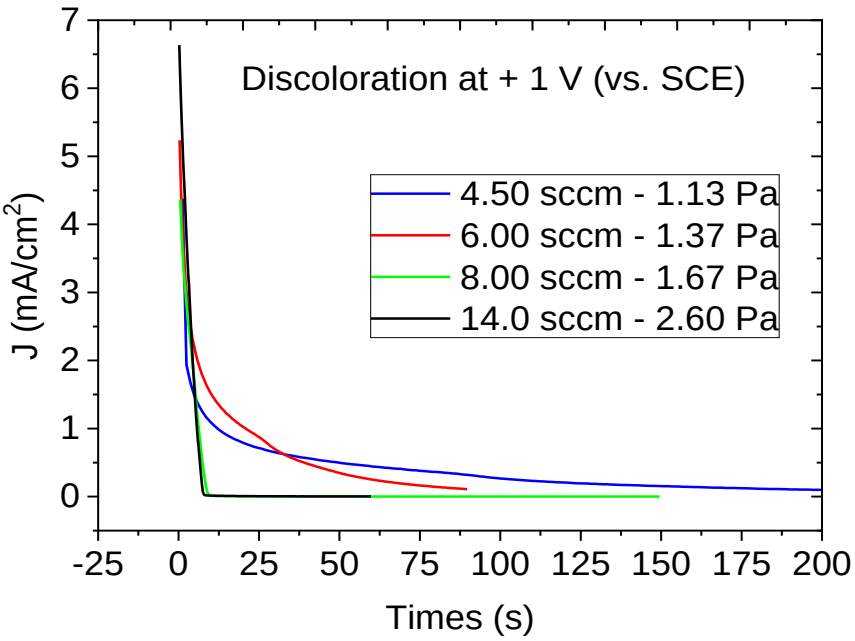
Discoloration at + 1 V (vs. SCE)
J (mA/cm2)
Times (s)
4.50 sccm - 1.13 Pa
6.00 sccm - 1.37 Pa
8.00 sccm - 1.67 Pa
14.0 sccm - 2.60 Pa

11 b

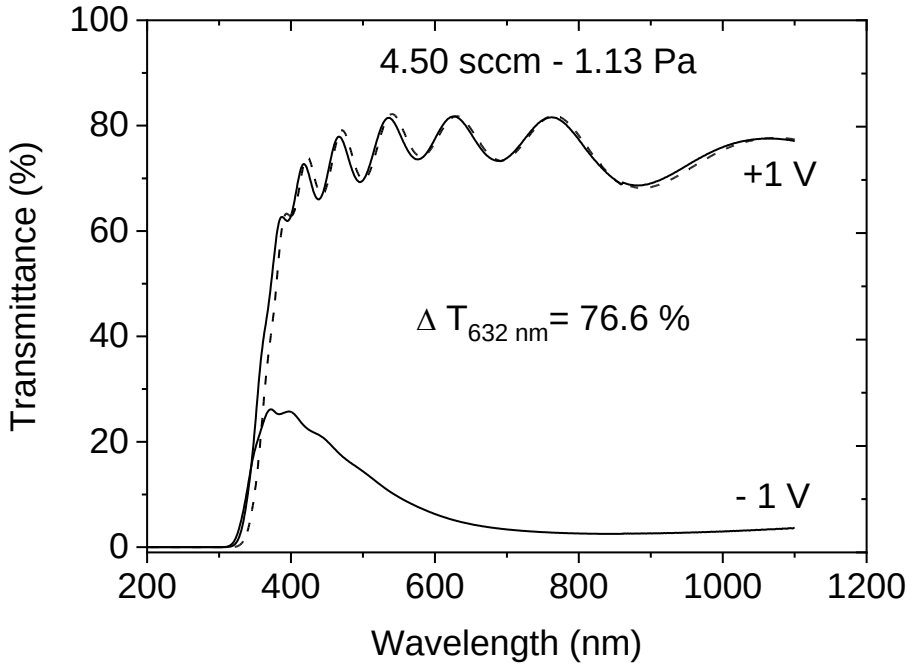
4.50 sccm - 1.13 Pa
+1 V
Δ T632 nm= 76.6 %
- 1 V
Transmittance (%)
Wavelength (nm)
0
20
40
60
80
100
200
400
600
800
1000
1200

12 a

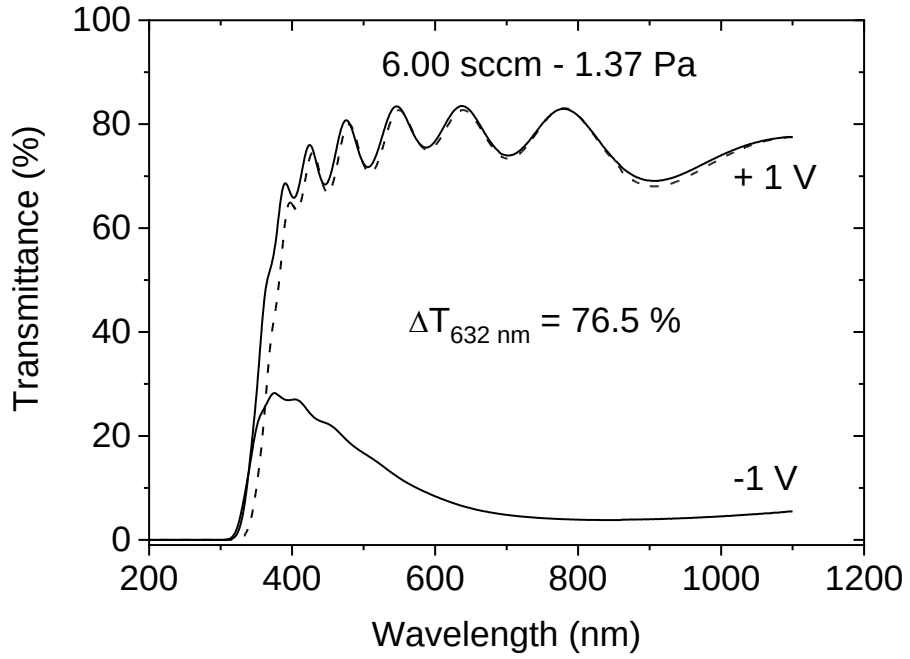
6.00 sccm - 1.37 Pa
+ 1 V
ΔT632 nm = 76.5 %
-1 V
Transmittance (%)
Wavelength (nm)
0
20
40
60
80
100
200
400
600
800
1000
1200

12 b

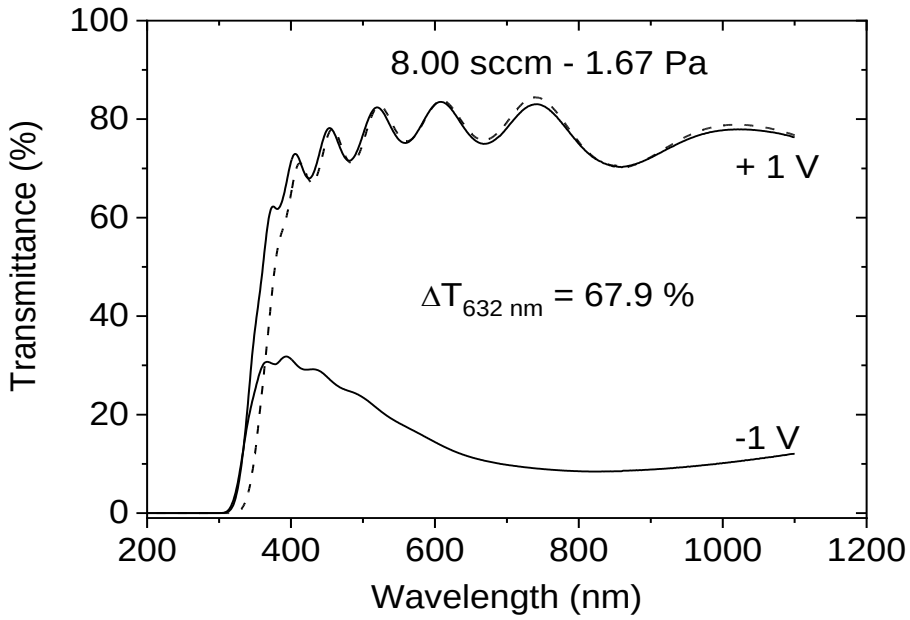
8.00 sccm - 1.67 Pa
+ 1 V
ΔT632 nm = 67.9 %
-1 V
Transmittance (%)
Wavelength (nm)
0
20
40
60
80
100
200
400
600
800
1000
1200

12 c

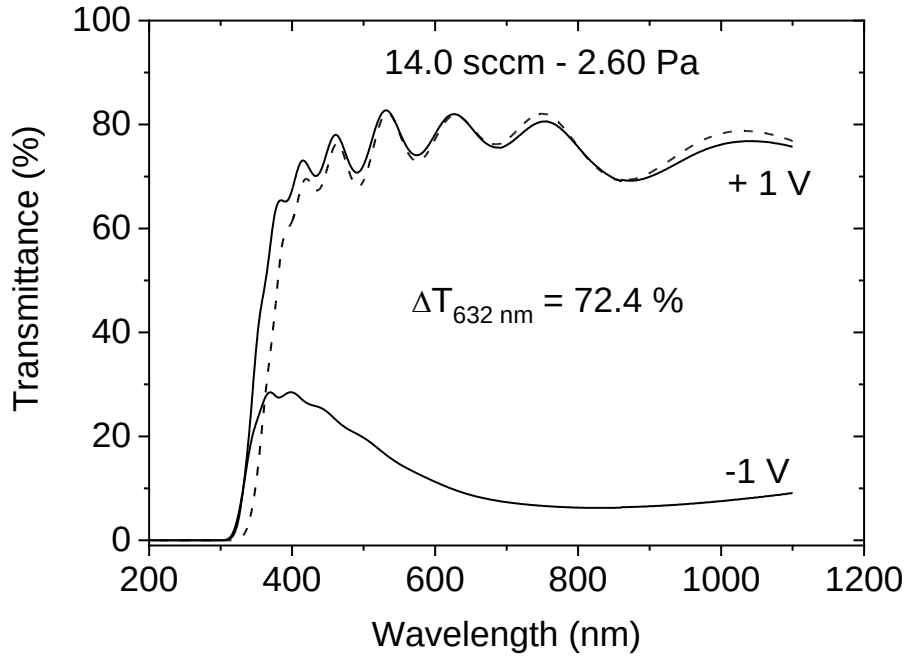
14.0 sccm - 2.60 Pa
+ 1 V
ΔT632 nm = 72.4 %
-1 V
Transmittance (%)
Wavelength (nm)
0
20
40
60
80
100
200
400
600
800
1000
1200

12 d

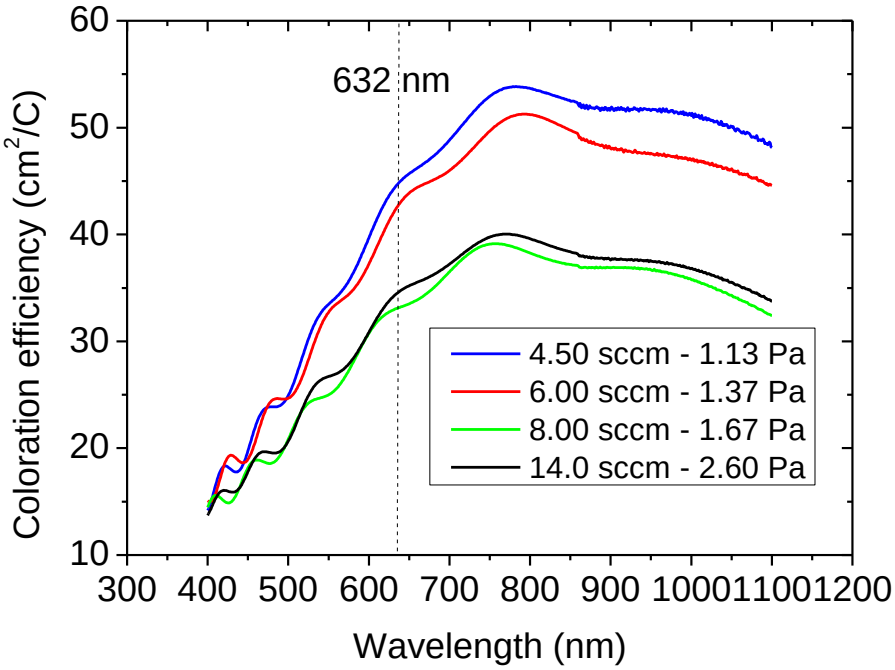
632 nm
Coloration efficiency (cm²/C)
Wavelength (nm)
4.50 sccm - 1.13 Pa
6.00 sccm - 1.37 Pa
8.00 sccm - 1.67 Pa
14.0 sccm - 2.60 Pa

13

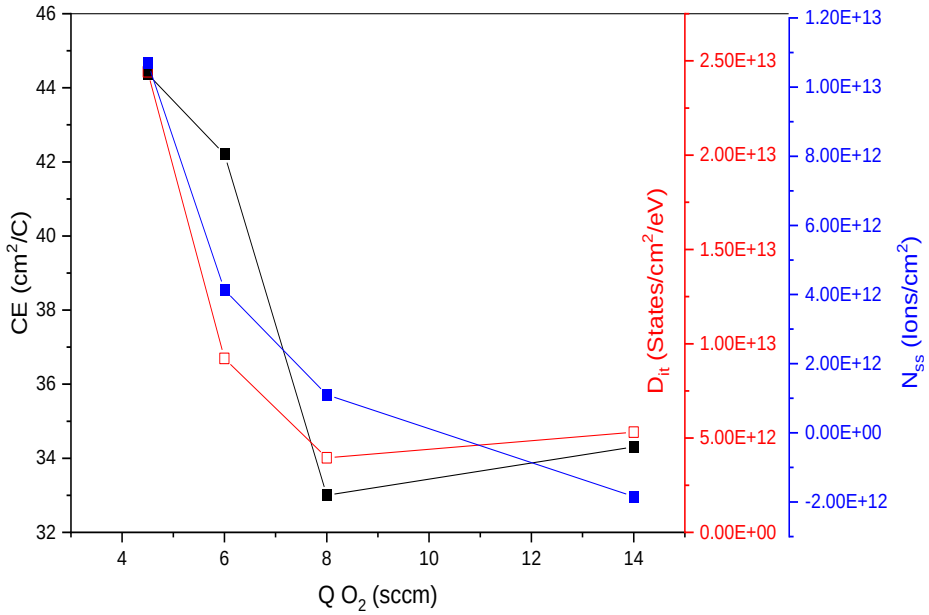
CE (cm²/C)
Q O₂ (sccm)
D_it (States/cm²/eV)
N_ss (Ions/cm²)

14